IJEAS

International Journal of Engineering & Applied Sciences

IJEAS

Abstracting & Indexing

Editorial Scope

The journal presents its readers with broad coverage across some branches of engineering and science of the latest development and application of new solution algorithms, artificial intelligent techniques innovative numerical methods and/or solution techniques directed at the utilization of computational methods in solid and nano-scaled mechanics.

International Journal of Engineering & Applied Sciences (IJEAS) is an Open Access Journal

International Journal of Engineering & Applied Sciences (IJEAS) publish original contributions on the following topics:

Civil Engineering: numerical modelling of structures, seismic evaluation, experimental testing, construction and management, geotechnical engineering, water resources management, groundwater modelling, coastal zone modelling, offshore structures, water processes, desalination, waste-water treatment, pavement and maintenance, transport and traffic, laser scanning, and hydrographic surveying, numerical methods in solid mechanics, nanomechanic and applications, microelectromechanical systems (MEMS), vibration problems in engineering, higher order elasticity (strain gradient, couple stress, surface elasticity, nonlocal elasticity)

Electrical Engineering: artificial and machine intelligence and robotics, automatic control, bioinformatics and biomedical engineering, communications, computer engineering and networks, systems security and data encryption, electric power engineering and drives, embedded systems, Internet of Things (IoT), microwaves and optics.

Engineering Mathematics and Physics: computational and stochastic methods, optimization, nonlinear dynamics, modelling and simulation, computer science, solid state physics and electronics, computational electromagnetics, biophysics, atomic and molecular physics, thermodynamics, geophysical fluid dynamics, wave mechanics, and solid mechanics.

Mechanical Engineering: machine design, materials science, mechanics of materials, manufacturing engineering and technology, dynamics, robotics, control, industrial engineering, ergonomics, energy, combustion, heat transfer, fluids mechanics, thermodynamics, turbo machinery, aerospace research, aerodynamics, and propulsion.

CONTENTS

Mechanical and Optical Properties of Multiwall Carbon Nanotube-Reinforced ZA27-Al₂O₃ Hybrid Composites Fabricated by Powder Metallurgy Routine

Mikail Aslan

Gaziantep University, Faculty of Engineering, Department of Metallurgical and Material Science Engineering, Gaziantep, 27310, Turkey

✉: mikailsln@gmail.com , 🆔*: 0000-0003-2235-5104-0000*

Abstract

In this study, multiwall carbon nanotubes (MWCNT) were employed as reinforcement elements in the hybrid composites of ZA27-Al2O3 produced through a powder metallurgy routine. The MWCNTs were incorporated at concentrations of 1%, 3%, and 5% in the samples. The preparation involved planetary ball milling for 4 hours, utilizing 10-diameter steel balls, followed by pressing the powders using a 20-ton capacity manual press machine after sintering at 400 °C. The composites' microstructures were analyzed using an optical microscope, and their densities were measured following the principle of Archimedes. Furthermore, the mechanical properties were evaluated by conducting Vickers hardness tests. The results indicate that the addition of MWCNTs resulted in an increase in hardness values. The sample with ZA27-Al2O3-5% MWCNT exhibited the highest hardness scale value

Keywords: Mechanical alloying, hybrid composites, ZA-27 zinc alloy, carbon nanotube.

1. Introduction

Zinc-Aluminum (ZA) alloys have gained popularity as metal matrix composites due to their exceptional strength, hardness, and wear resistance. These qualities position them as viable alternatives to traditional materials such as aluminum, brass, bronze, or iron for designers working on structures and machine parts. Consequently, the increasing utilization of ZA alloys across various industrial applications (,such as automotive, building, sporting goods, toys, hardware, decoration and white goods[1]) is becoming a notable trend[2]. Moreover, ZA-27-based composites have emerged as a cutting-edge generation of metal matrix composites, showcasing the potential to fulfill the evolving demands of advanced engineering in bearing and bushing applications[3]. Nevertheless, the alloyed system does exhibit certain limitations, notably its diminished performance at elevated temperatures exceeding 120°C and a relatively high coefficient of thermal expansion[4]. One of the possible solutions for overcoming these deficiencies is the reinforcement of the ZA alloy by incorporation of a thermally stable second phase[5]. To address these shortcomings, one potential approach is the incorporation of a thermally stable second phase to reinforce the ZA alloy. This strategy has proven successful in enhancing the properties of aluminum-based alloys through the addition of ceramic particles. Consequently, a growing number of researchers have been drawn to explore the production and analysis of ceramic-reinforced composites[6-10].

Incorporating hard and thermally stable ceramic reinforcements into ZA alloys significantly enhances their hardness[11], elastic modulus[12], and reduces the coefficient of thermal expansion at ambient temperature. Furthermore, as the content of the reinforcing phase increases, there is a continuous improvement in the properties of the composite material. The increase in

hardness could be accompanied by[5] or without a decrease in strength[13]. Kumar et. al[14] reported zirconium diboride (ZrB_2) reinforced zinc aluminum-based alloys. Results indicate the mechanical properties of the composites were improved. At 9 vol% of ZrB_2, the matrix grains are refined by 48%, and the hardness value is improved by 68% compared to pure ZA alloy. Khan et al[15] studied titanium carbide (TiC)-reinforced ZA-27 alloy composites prepared by using the powder + liquid metallurgy route. It was observed that increasing the TiC reinforcement content from 5 wt % to 10 wt % results in improved wear resistance in the ZA-based composite[16].

Hybrid metal matrix composites (HMMCs) are second-generation composites where more than one type, shape, and size of reinforcements are used to obtain better properties[17]. Hybrid composites possess better properties compared with single-reinforced composites as they combine the advantages of their constituent reinforcements. A study conducted by Marigoudar[18] depicts an experimental model for investigating the mechanism and nature of chip formation during the machining of silicon carbide (SiC)-reinforced mono and SiC and graphite-reinforced ZA43 HMMCs. It was observed that hybrid composite being more brittle than mono composite material produces short segmental chips. the work is concentrated on the production of ZA-27 alloy and hybrid composite reinforced with 1.5 weight percentage of SiC and 0.5 weight percentage of graphite (Gr). The ultrasonic-assisted stir casting method is used for the preparation of the ZA-27/SiC/Gr hybrid metal matrix composite. The mechanical properties of the hybrid composite increase as compared to the base metal.

Specifically, carbon nanotubes can be utilized as reinforcing elements in composites due to their exceptional properties[19-28]. A carbon nanotube is a unique form of carbon structure, exhibiting both elasticity and flexibility, yet possessing remarkable hardness, being ten times stronger than steel. It also boasts excellent electrical conductivity and an impressive melting point exceeding 3550°C, which piques interest for its diverse applications in mechanical, electrical, and thermal realms. Leveraging its exceptional mechanical properties, carbon nanotubes serve as an ideal reinforcement in metal composites.

In this study, we present the first-ever production of multi-wall carbon nanotube (MWCNT)-reinforced zinc-based hybrid composites through a mechanical alloying routine. We investigate the impact of varying MWCNT ratios on the resulting HMMCs. Additionally, we conduct microstructural, density, and mechanical analyses to gain comprehensive insights into the performance of these innovative materials.

2. Materials and Method

To create MWCNT-reinforced zinc-alumina-based hybrid alloys, elemental powder precursors of Al, Zn, Cu, Al2O3, and MWCNT were initially employed. The composition of the zinc alloy resembled ZA-27 zinc alloy. The mechanical alloying process was carried out using a Retsch PM-100 model planetary high-energetic ball mill with 120 mL stainless steel grinding jars rotating at 250 rpm. The milling direction was reversed after every 7 minutes, and the total milling duration was 4 hours. The ball-powder weight ratio was maintained at 7:1, with 10 mm diameter stainless steel balls. To prevent overheating, the planetary mill was paused for 2 minutes after every 5 minutes of operation. Additionally, 5 ml of water was used as a wet medium agent. To achieve a homogenous distribution, the powder samples underwent 10 minutes of mechanical stirring and were then cold pressed in a steel die at 200 MPa to form bulk alloys. The bulk samples were subsequently sintered at 400 °C for 2 hours, followed by immediate cooling at room temperature.

3. Results and Discussion

Aluminum (99.9% purity, ~44 μm), zinc (99.8% purity, ~44 μm), and copper (99.9% purity, ~44 μm) powders were procured from Nanografi, while Al2O3 powders (99.9% purity, ~44 μm) were supplied by EGE Nano A.Ş. The chemical composition of the ZA-27 alloy is outlined in Table 1.

Table 1. Bulk chemical composition of ZA-27 alloy

Al(%)	Cu(%)	Zn(%)
27	2.5	70.5

In this experimental study, a powder mixture of ZA-27 and Al2O3 was employed as the matrix material, while multi-wall carbon nanotubes (MWCNT) served as the reinforcing element. The technical properties of the MWCNT can be found in Table 2. The weight ratio of ZA-27 alloy to Al2O3 was maintained at 10:1.

Table 2. Some technical properties of MWCNT

Multiwalled carbon nanotubes	
Purity (%)	>96
Density (True) (g/cm^3)	2.4
Outer diameter (nm)	8–18
Surface area (m^2 /g)	>210
Inner diameter (nm)	5–10
Length (μm)	10–35
Density (tap) (g/cm^3)	0.3

To fabricate the MWCNT-reinforced Al-Zn-Mg-Cu composites, MWCNTs were incorporated at weight percentages of 1%, 3%, and 5%. The densities of the investigated materials were determined using the Archimedean principle. The measured density of the composites with varying MWCNT weight percentages is illustrated in Figure 1, showcasing a decrease in density with the addition of MWCNTs. These findings align with a similar study conducted by Garg et al.[29]. The incorporation of graphene into aluminum composites resulted in a reduction in their density values. This phenomenon can be attributed to the decreased intergranular friction forces between graphene and other elements. Interestingly, the density values exhibited a further decrease after the sintering process (refer to Figure 1). This behavior can be rationalized by considering the densification stage, where the elimination of unstable materials creates opportunities for the formation of internal pores with varying volumes and shapes. During this process, small pores and/or concave surface morphologies have the ability to shrink through mass transfer via inward atomic diffusion from the particle's bulk towards the pore surface. This mechanism effectively fills the pore space. In contrast, large pores and/or convex surface morphologies are unable to shrink as mass transfer is dominated by outward atomic diffusion from the pore surface towards the particle's bulk. This dominance enlarges the pore space, resulting in what is commonly referred to as the foaming process, ultimately leading to a reduction in density.
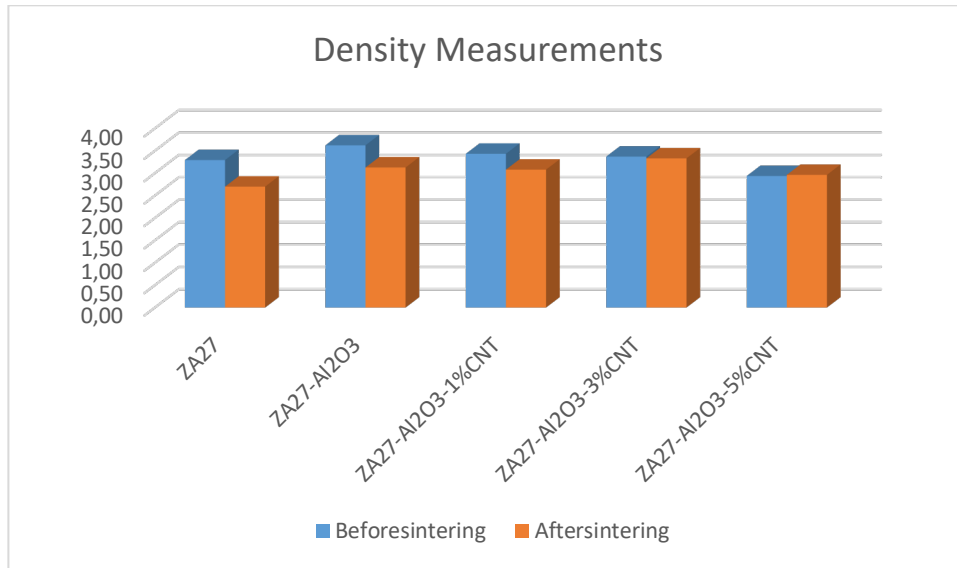
Fig. 1. Measured density of the given materials

The metallographic processes, including sanding, polishing, and etching, were employed sequentially. The sanding technique involved the use of 1000 and 2000 mesh sanders to treat the material surfaces. Subsequently, the specimens were polished using 6 μ diamond suspension followed by 3 μ diamond suspension to achieve a smoother finish. Finally, the samples underwent the etching process using diluted nitrate solutions.

For hardness testing of the studied composites, measurements were performed using an AOB Vickers Microhardness tester with a load of 0.5 kgf and a dwell time of 15 seconds. Five indentations were made for each sample, and the mean hardness values were recorded. The Vickers hardness values are presented in Figure 2. Notably, the hybrid composite (ZA27-Al2O3) exhibited a 7% higher hardness compared to the pure alloy. The addition of MWCNTs significantly increased the hardness values. However, it was observed that the MWCNTs were not uniformly distributed throughout the structure, particularly evident in the ZA27-Al2O3-3% MWCNT composite (refer to Figure 2), where a decrease in hardness value was observed in comparison to the ZA27-Al2O3-1% MWCNT composite.
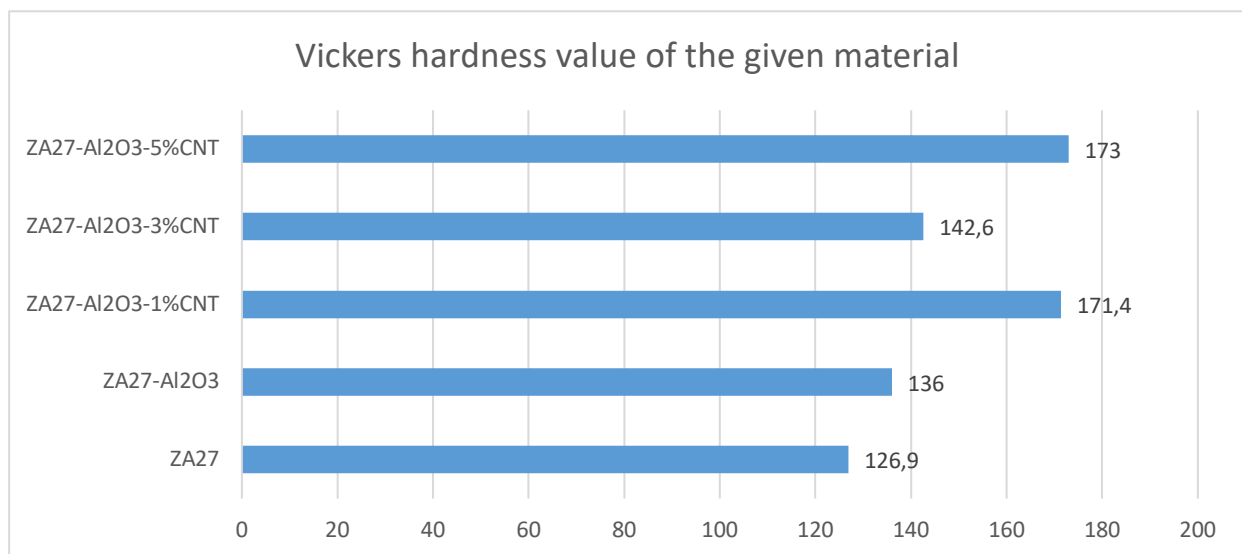
Fig. 2. Vickers hardness values of the given materials

Figure 3 presents the optical images of the analyzed structures. A comparison with Figure 6 (c-e) reveals a noticeable refinement of the grain boundaries. This observation aligns with previous studies on the subject [30]. Furthermore, it can be observed that agglomerations are present in several regions, with dense MWCNT reinforcement particles clustering around and adhering to the surfaces of ZA27 and Al2O3 particles. These agglomerations have a detrimental effect on the mechanical properties of the materials, which is consistent with the findings from the Vickers hardness tests.

a) ZA27

b)ZA27-Al$_2$O$_3$

c) ZA27-Al$_2$O$_3$-%1MWCNT

d) ZA27-Al$_2$O$_3$-%3MWCNT

e) ZA27-Al$_2$O$_3$-%5WCNT
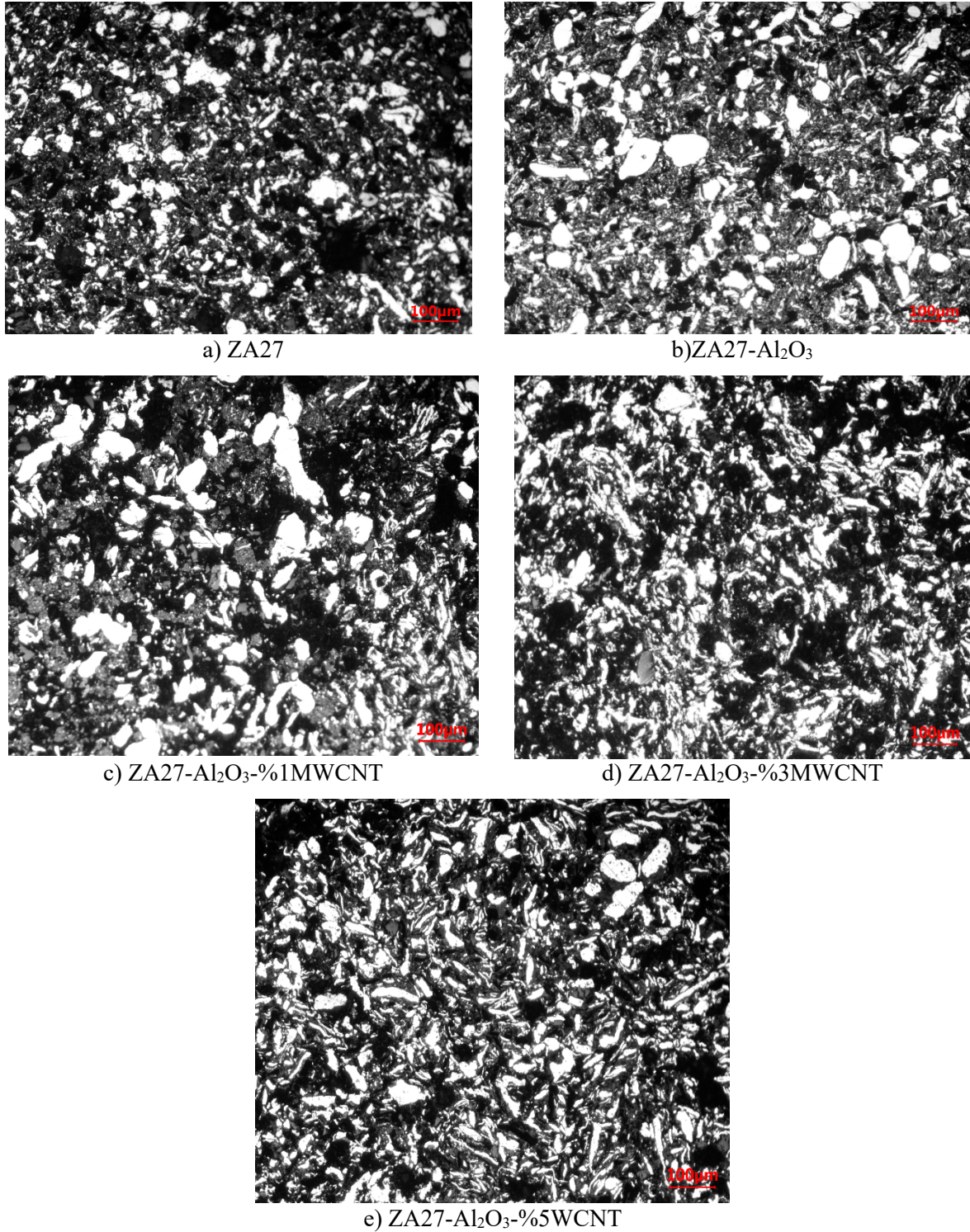
Fig. 3. Optical microscope images of the given materials

4. Conclusion

This study focused on the fabrication of zinc-based hybrid composites reinforced with multi-wall carbon nanotubes (MWCNTs) using a powder metallurgy routine. ZA-27 and Al2O3 were chosen as the matrix materials, while MWCNTs were employed as the reinforcing element. The primary objective was to investigate the impact of varying MWCNT ratios on the properties of the hybrid metal matrix composites.

The incorporation of MWCNTs resulted in a reduction in density values, which can be attributed to the diminished intergranular friction forces between the MWCNTs and other elements within the composite. Surprisingly, the sintering process further contributed to decreased density, contrary to its intended purpose. This phenomenon can be explained by the loss of unstable materials during densification, leading to the formation of internal pores with distinct volumes and shapes.

To evaluate the hardness properties of the composites, measurements were conducted using an AOB Vickers Microhardness tester with a load of 0.5 kgf and a dwell time of 15 seconds. The hardness values of the ZA27-Al2O3 composites were found to be 7% higher compared to those of the pure alloy, highlighting the reinforcing effect of alumina. Additionally, the introduction of MWCNTs significantly enhanced the hardness values.

Optical examination of the studied structures revealed that an increase in the MWCNT ratio resulted in finer grain boundaries. Furthermore, prominent agglomerations of dense MWCNT reinforcement particles were observed in various regions, adhering to the surfaces of ZA27 and Al2O3 powders. These agglomerations contributed to a decrease in the hardness values of the powders, consistent with the findings from the Vickers hardness tests.

References

[1] Pul M, Effect of sintering temperature on pore ratio and mechanical properties of composite structure in nano graphene reinforced ZA27 based composites. *International Journal of Minerals, Metallurgy Materials Science*, 27, 232-243, 2020.

[2] Petrica M, Badisch E, Peinsitt T, Abrasive wear mechanisms and their relation to rock properties. *Wear*, 308, 86-94, 2013.

[3] Owoeye SS, Folorunso DO, Oji B, Borisade SG, Zinc-aluminum (ZA-27)-based metal matrix composites: a review article of synthesis, reinforcement, microstructural, mechanical, and corrosion characteristics. *The International Journal of Advanced Manufacturing Technology*, 100, 373-380, 2019.

[4] Prasad B, Abrasive wear characteristics of a zinc-based alloy and zinc-alloy/SiC composite. *Wear*, 252, 250-263, 2002.

[5] Modi O, Rathod S, Prasad B, Jha A, Dixit G, The influence of alumina particle dispersion and test parameters on dry sliding wear behaviour of zinc-based alloy. *Tribology international*, 40, 1137-1146, 2007.

[6] Gangwar S, Pathak VK, Dry sliding wear characteristics evaluation and prediction of vacuum casted marble dust (MD) reinforced ZA-27 alloy composites using hybrid improved bat algorithm and ANN. *Materials Today Communications*, 25, 101615, 2020.

[7] Girish B, Prakash K, Satish B, Jain P, Devi K, Need for optimization of graphite particle reinforcement in ZA-27 alloy composites for tribological applications. *Materials Science Engineering: A*, 530, 382-388, 2011.

[8] Sastry S, Krishna M, Uchil J, A study on damping behaviour of aluminite particulate reinforced ZA-27 alloy metal matrix composites. *Journal of Alloys Compounds*, 314, 268-274, 2001.

[9] Sharma S, Girish B, Kamath R, Satish B, Effect of SiC particle reinforcement on the unlubricated sliding wear behaviour of ZA-27 alloy composites. *Wear*, 213, 33-40, 1997.

[10] Sharma S, Girish B, Somashekar D, Satish B, Kamath R, Sliding wear behaviour of zircon particles reinforced ZA-27 alloy composite materials. *Wear*, 224, 89-94, 1999.

[11] Karni N, Barkay G, Bamberger M, Structure and properties of metal-matrix composite. *Journal of Materials Science Letters*, 13, 541-544, 1994.

[12] Zhu H, Liu S, Mechanical properties of squeeze-cast zinc alloy matrix composites containing α-alumina fibres. *Composites*, 24, 437-442, 1993.

[13] Miroslav B, Mitrović S, Zivic F, Bobić I, Wear behavior of composites based on ZA-27 alloy reinforced by Al2O3 particles under dry sliding condition. *Tribology Letters*, 38, 337-346, 2010.

[14] Kumar V, Gautam G, Yadav AK, Mohan A, Mohan S, Influence of InSitu Formed ZrB2 Particles on Dry Sliding Behavior of ZA Based Metal Matrix Composites. *International Journal of Metalcasting*, 17, 1-15, 2022.

[15] Khan MM, Nisar M, Effect of in situ TiC reinforcement and applied load on the high-stress abrasive wear behaviour of zinc–aluminum alloy. *Wear*, 488, 204082-204097, 2022.

[16] Kumar NS, Mechanical and wear behavior of ZA-27/Sic/Gr hybrid metal matrix composites. *Materials Today: Proceedings*, 5, 19969-19975, 2018.

[17] Mahendra K, Radhakrishna K, Characterization of stir cast Al—Cu—(fly ash+ SiC) hybrid metal matrix composites. *Journal of Composite Materials*, 44, 989-1005, 2010.

[18] Marigoudar RN, Chip profile studies on SiC reinforced mono and SiC and graphite reinforced hybrid ZA43 MMCs. *Advances in Materials Processing Technologies*, 1-13, 2022.

[19] Aydogdu M, Arda M, Torsional vibration analysis of double walled carbon nanotubes using nonlocal elasticity. *International Journal of Mechanics Materials in Design*, 12, 71-84, 2016.

[20] Civalek Ö, Akbaş ŞD, Akgöz B, Dastjerdi S, Forced vibration analysis of composite beams reinforced by carbon nanotubes. *Nanomaterials*, 11, 571, 2021.

[21] Mercan K, Numanoglu H, Akgöz B, Demir C, Civalek Ö, Higher-order continuum theories for buckling response of silicon carbide nanowires (SiCNWs) on elastic matrix. *Archive of Applied Mechanics*, 87, 1797-1814, 2017.

[22] Peng T, Chang I, Mechanical alloying of multi-walled carbon nanotubes reinforced aluminum composite powder. *Powder Technology*, 266, 7-15, 2014.

[23] Akgöz B, Civalek Ö, Investigation of size effects on static response of single-walled carbon nanotubes based on strain gradient elasticity. *International Journal of Computational Methods*, 9, 1240032, 2012.

[24] Uzun B, Kafkas U, Yaylı MÖ, Free vibration analysis of nanotube based sensors including rotary inertia based on the Rayleigh beam and modified couple stress theories. *Microsystem Technologies*, 27, 1913-1923, 2021.

[25] Büşra U, Yayli MÖ, A solution method for longitudinal vibrations of functionally graded nanorods. *International Journal of Engineering Applied Sciences*, 12, 78-87, 2020.

[26] Jena SK, Chakraverty S, Malikan M, Mohammad-Sedighi H, Hygro-magnetic vibration of the single-walled carbon nanotube with nonlinear temperature distribution based on a modified beam theory and nonlocal strain gradient model. *International Journal of Applied Mechanics*, 12, 2050054-2050065, 2020.

[27] Uzun B, Kafkas U, Yaylı MÖ, Stability analysis of restrained nanotubes placed in electromagnetic field. *Microsystem Technologies*, 26, 3725-3736, 2020.

[28] Belarbi M-O, Salami SJ, Garg A, Daikh A-A, Houari M-S-A, Dimitri R, et al., Mechanical behavior analysis of FG-CNT-reinforced polymer composite beams via a hyperbolic shear deformation theory. *Continuum Mechanics Thermodynamics*, 35, 497-520, 2023.

[29] Garg P, Gupta P, Kumar D, Parkash O, Structural and mechanical properties of graphene reinforced aluminum matrix composites. *Journal of Materials and Environmental Science*, 7, 1461-1473, 2016.

[30] Muharrem P, Karbon Nanotüp takviyeli ZA-27 Esaslı Kompozitlerde Karbon Nanotüp Takviye Oranının Mikroyapı Ve Bazı Mekanik Özelliklere Etkisi. *International Journal of Engineering Research*, 12, 307-316, 2020

Behavior of Composite Parts Adhesively Joined with Single Lap Joint and Intermediated Material Under Tensile Load

İsmail Yasin Sülü

İnönü University, Department of Mechanical Engineering, Malatya, Turkey

✉: ismail.sulu@inonu.edu.tr , 🆔: *0000-0002-2648-6294*

Abstract

In research, composite parts adhesively joined with single-lap joint (SLJ) and intermediated material under tensile load were examined by finite element analysis (FEA). While T700 Carbon/epoxy was used for composite parts and intermediate material, DP 410 type was preferred for adhesive. The numerical studies were carried out by ANSYS 14.5 based on finite elements method. The von-Mises failure criteria and the Tsai-wu failure criteria were respectively considered for adhesive and composites. The analyses were firstly actualized to determine the failure loads for each parameter situation. The stresses at obtained failure load for each parameter state were investigated. The critical equivalent stresses on adhesive layers were examined and the critical stress lines for length and width was determined. The distributions of normal and shear stresses in all directions were obtained by considering critical stress line on adhesive layers. Similarly, the von-Mises stress distributions were obtained. Considering critical stress lines, the stress distributions on width and length of overlap dimensional were compared. The effects of overlap dimensional, orientation angle and intermediated material on effect of joint zone were investigated.

Keywords: Intermediated material, finite element analysis, orientation angles, stress analysis, adhesive, joint design.

1. Introduction

Composite materials is preferred many industries, such as aircraft, aerospace, automotive, marine, sport equipment and various areas such as lightweight and excellent structural performance [1-3].The use of adhesive bonding for combining structures as different from other conventional methods is created many advantages. It enables a simple and efficient joint procedure while obtaining any weight decrease and limiting material failure [4]. Also, due to easy application and good mechanical properties of adhesives, there is also an increasing demand for adhesives for repairing and joining damaged parts [5].

Adhesive applications are widely used to be joined many materials. Important factors in bonding processes are the working life and strength of the joined area. Therefore, many researches about joint design are carried out. Single-lap joint (SLJ) joining techniques are also used in composite-metal connections in different loading situations. When the effect of the adhesive to different types of materials cannot be similar, it will show different mechanical behavior as a result of combining different materials [6-8]. Moreover, different studies on SLJ are available in the literature. Shang and et al. [9] fabricated and tested SLJs with a hard and brittle adhesive. It was shown that SLJs joined with the tough adhesive failed by interlaminar delamination in the CFRP, SLJs bonded with the brittle adhesive failed cohesively in the adhesive. In a study on joint lifetimes, tensile tests were actualized on the SLJs to define the highest loads for fatigue tests and also to evaluate their quasi-static behaviors. They determined fatigue loads according to the test results and conducted studies at different adherents thicknesses. Also, they determined the fatigue

loads according to the test results and conducted studies on the strength of SLJs with different adherents thicknesses [10].

Moreover, Huang and et al. [11] investigated the influence of temperature, impact energy and stiffness combination on residual tensile properties. It was noted that both temperature and impact energy now have a strong correlation with the static properties, and decreasing the relative stiffness ratio can decrease the residual tensile strength of SLJs. In another study, Shi and et al. [12] carried out numerical studies and experimental on the FT durability of basalt FRP (BFRP) SLJs. It was noted that the tensile properties of different BFRPs were not affected by FT cycling, while significant deterioration was seen for the bonding behavior of the epoxy resin and fiber-matrix interface. Choudhury and Debnath [13] have experimentally examined mechanical characterization of adhesively joined SLJ of green composites under tensile and compressive loads. They found that increasing the overlap length dimensions positively affects the mechanical performance. Moreover, there were studies on the joining of different materials using the single-lap joint method and the mechanical performance of the joint area. In most studies, parameters such as different overlap sizes, adhesive thickness, different loadings, adhesive type and orientation angle of composites have been taken into account [13-20].

In this investigative, composite plates adhesively joined with SLJ and intermediated materials were investigated by non-linear FEA. In this joint design, composite layer between adhesive layers were put into. Failure loads were obtained for parameters such as over-lap dimensional and orientation angles. Due to be important the adhesive zone, shear stresses, stresses at all directions and the equivalent stress on adhesive layers were determined at the time of the failure. The aim of the research is to demonstrate that the adhesive is easy to use, high strength and more practical in composite plates for the industry.

2. 3-D Finite Element Modeling

Composite plates bonded with intermediated material under tensile load were presented in Fig. 1. Composite adherends were eight layered, intermediated material was one layered composite. Composites and adhesive were considered carbon/epoxy (T700) and DP 410 respectively. The material constants of adhesive in Table 1 and composites Table 2 were presented. The parameters in Table 3 were considered for orientation angles. The σ-ε behavior of adhesive was shown in Fig. 2.

The each layer thickness and the thickness of intermediated composite material were 0.2 mm (t), the total thickness of composite plates was 8 x t, and the thickness of adhesive layer was 0.2 mm (t1). The lengths (L) of the composite parts were 62.5 mm, the over-lap lengths (L1) and widths were 15 mm, 20 mm, 25 mm. Orientation angle of intermediated composite material was considered Type I for all joints.

Table 1. Material properties for DP 410 adhesive [18-22]	
Properties	DP 410
Young's modulus E_a (MPa)	2567.45
Poisson's ratio v_e	0.31
Yield strength σ_y (MPa)	38
Ultimate tensile strength σ_t (MPa)	40.79
Ultimate tensile strain ε_t (mm·mm^{-1})	0.027
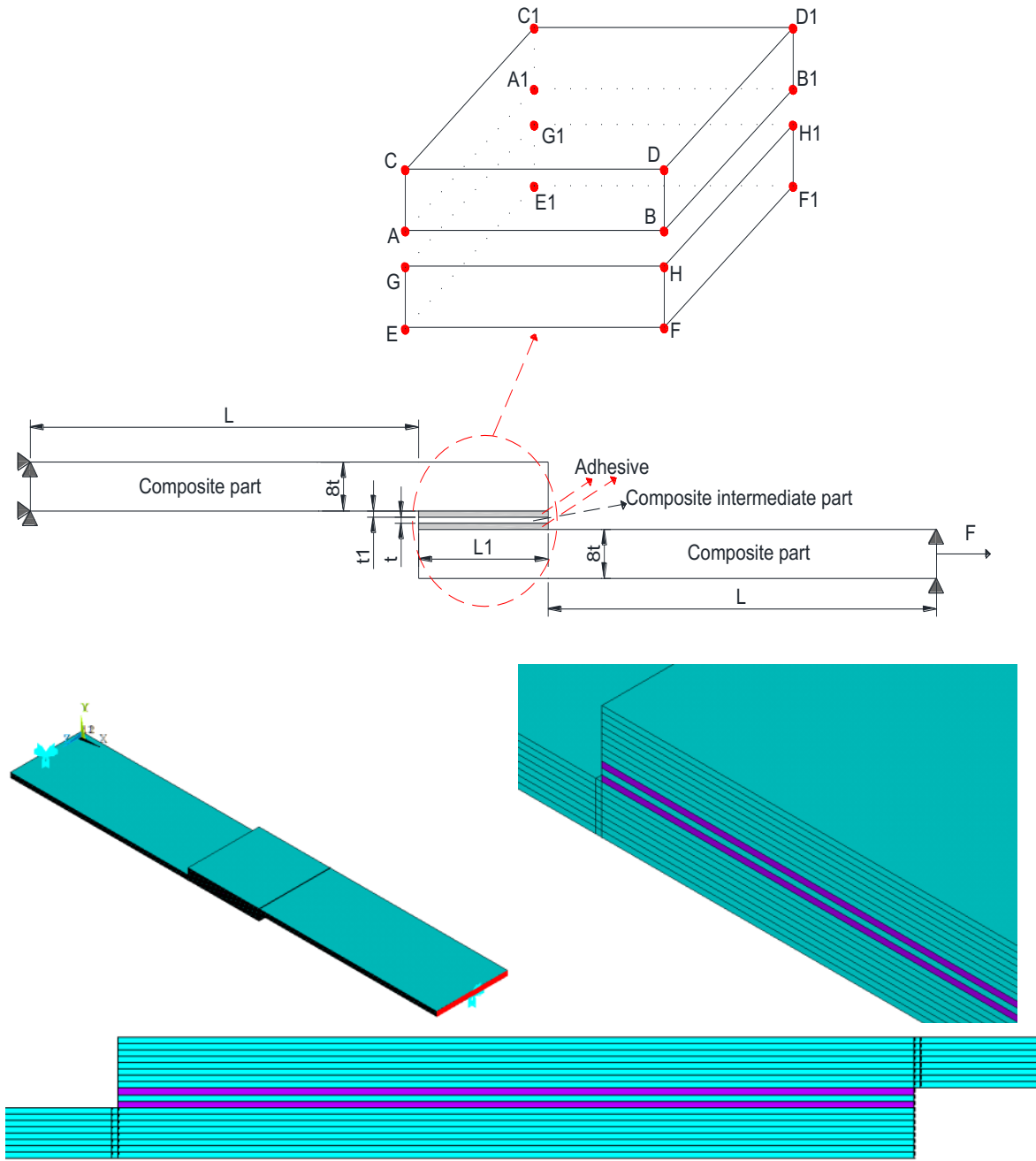
Fig. 1.Composite plates joined with SLJ and intermediated material

In the non-linear FEM, composite plates bonded with SLJ and intermediated materials were simulated via FEM. 3D-FEM was generated during the analysis of joint with SLJ and intermediated materials. In the model, SOLID186 was considered in the macro ANSYS 14.5 version generated. Its properties were 20 node isoperimetric quadrangular elements and three degrees of freedom for each node in all directions. One end of plates jointed was fixed nodal in all directions, other one was fixed in y and z directions. In Fig. 3, the joint design configuration, detailed mesh status and boundary conditions considered in research were presented. Failure analyses were realized for joints with SLJ and intermediated materials. The von-Mises failure criteria and Tsai-wu failure criteria were respectively considered for the adhesive and the composite [18-22].

Table 2. Material properties for T700 [23]

Properties	Carbon/epoxy (T700)
E_x (MPa)	132000
E_y (MPa)	10300
E_z (MPa)	10300
G_{xy}(MPa)	6500
G_{yz}(MPa)	3910
G_{xz} (MPa)	6500
v_{xy}	0.25
v_{yz}	0.38
v_{xz}	0.25
T_x (MPa)	2100
T_y (MPa)	24
T_z (MPa)	24
C_x (MPa)	1050
C_y (MPa)	132
C_z (MPa)	132
S_{xy}(MPa)	75
S_{yz}(MPa)	75
S_{xz}(MPa)	75

Table 3. Angle parameters

Orientation angles(^{0})	
[0/ 0/ 0/ 0/ 0/ 0/ 0/ 0]	Type I
[15/ -15/ 15/ -15/ 15/ -15/ 15/ -15]	Type II
[30/ -30/ 30/ -30/ 30/ -30/ 30/ -30]	Type III
[45/ -45/ 45/ -45/ 45/ -45/ 45/ -45]	Type IV
[60/ -60/ 60/ -60/ 60/ -60/ 60/ -60]	Type V
[75/ -75/ 75/ -75/ 75/ -75/ 75/ -75]	Type VI
[90/ 90/ 90/ 90/ 90/ 90/ 90/ 90]	Type VII
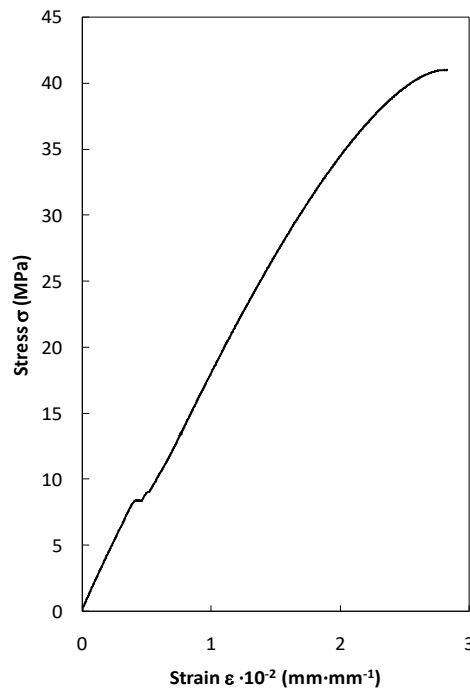
Fig. 2.Tensile stress–strain curve of DP 410 [18-22]
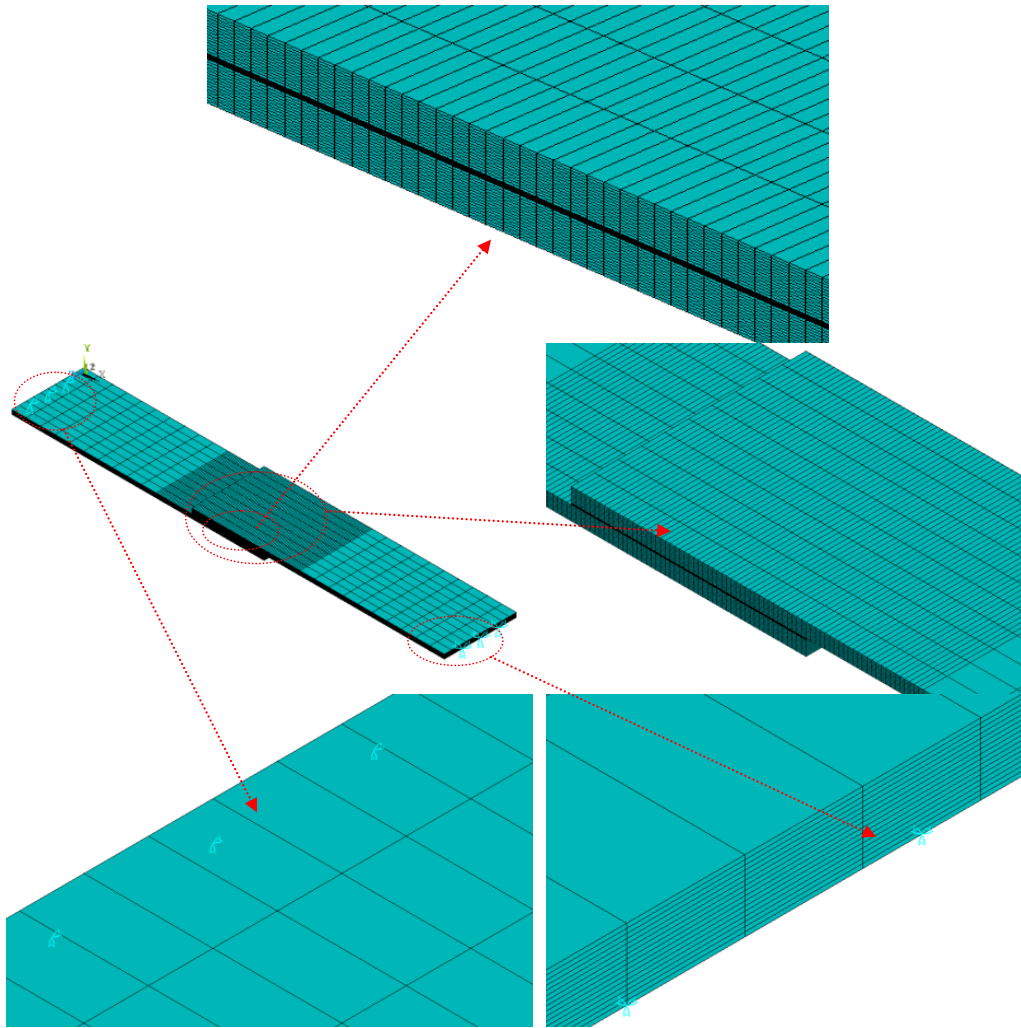
Fig. 3.Detailed mesh structure and boundary conditions on the model

3. Results and Discussion

3.1. Influence on stress distributions of L1 lengths and angles

Stress distributions of joint with SLJ and intermediate material were researched, the analysis was realized considering the dimensional and all orientation angles parameters of the 20 mm strap joint. Failure always created on composite parts, but the strength of the adhesion surfaces of the adhesive is important in bonding processes. Therefore, bond-lines on the adhesive in the joint region (Fig. 1) were considered. In order the determination of critical lines on joint region, σ_{eqv} distributions of the all lines on adhesive layers were checked. The σ_{eqv} on C-D and D-D1 were presented both maximum in Fig. 4a and Fig. 4b. So, the stresses were investigated for the C-D line on edges and the D-D1 line on width.
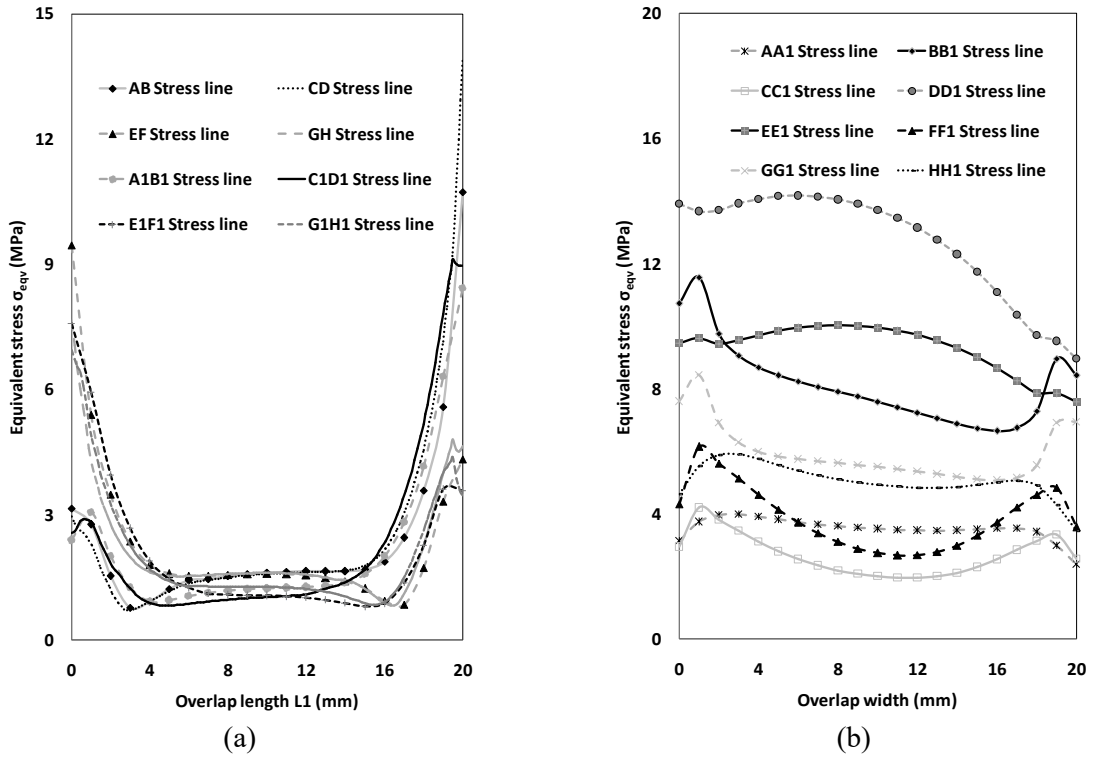
Fig. 4. Comparison the equivalent stresses throughout all lines (Fig. 1) for 20 mm of L1 and Type IV, a) On edges, b) On width

The stress behaviors of the joints with intermediated material and SLJ were given in Figs. 5 to 6. The stresses on critical lines of joint were generally maximum at the C-D on edge and the D-D1 on width. This was because the composite part on which the loading was made and the C-D and D-D1 lines on the adhesive were directly exposed to the damage load.

Due to be critical area adhesive layers, the distributions of σ_x, σ_y, σ_z, σ_{xy}, σ_{xz}, σ_{yz} and σ_{eqv} on adhesive were determined at damage loads. When Figs. 5 to 6 were investigated, the stresses were shown that were determined on critical lines as a result of joints with SLJ and intermediated material.

In Figs. 5 to 6, the actions of angles on the adhesive layers were presented. It could be said that σ_x, σ_y, σ_z, σ_{xy} and σ_{eqv} on critical line was the highest when composite parts with Type VII were used. σ_{yz} was the highest when joints with Type V were used. The σ_{xz} was the highest when joints with Type VI orientation angles were considered.
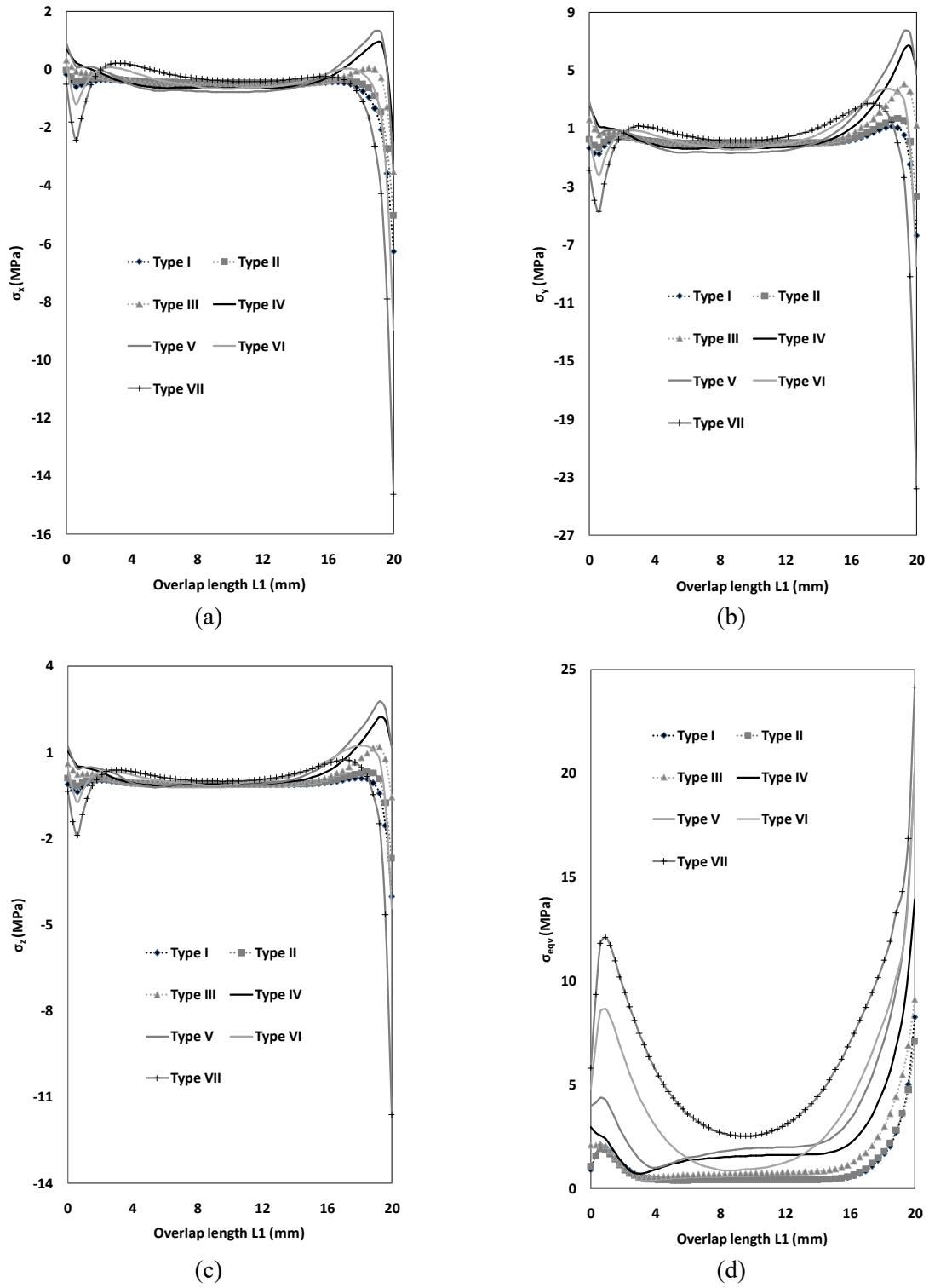
Fig. 5.Comparison of stresses for all orientations throughout C-D for 20 mm of L1, a) In x-direction, b) In y-direction, c) In z-direction, d) Equivalent stress σ_{eqv}

(a)

(b)

(c)
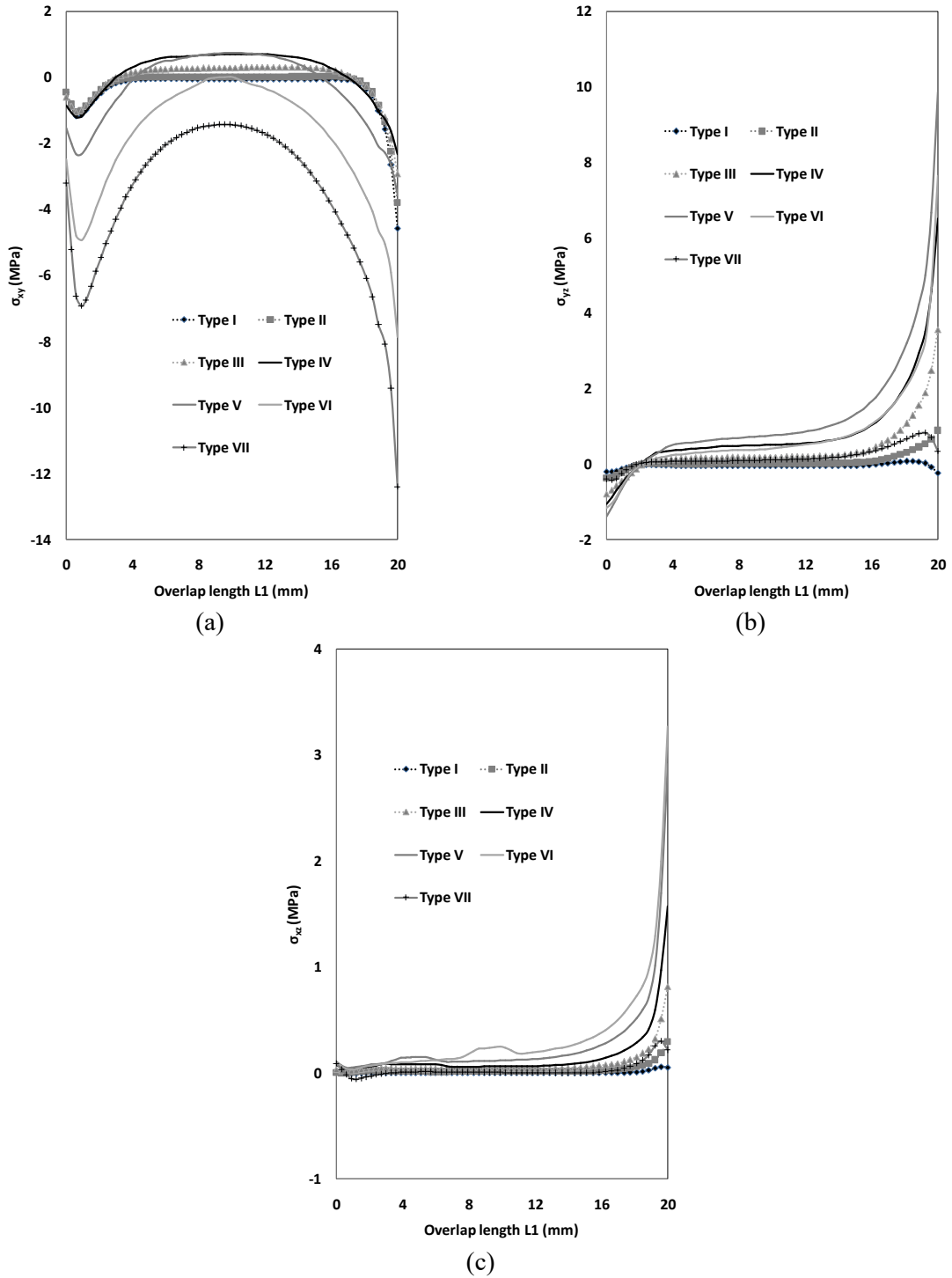
Fig. 6. Comparison of shear stresses for all orientations throughout C-D for 20 mm of L1, a) σ_{xy},b) σ_{yz},c) σ_{xz}

The σ_{eqv} stresses on C-D and D-D1 were examined in Fig. 7. Stress values in C-D and D-D1 stress lines for each orientation angles were compared together on the same graphs. While there was a regular stress distribution in the C-D and D-D1 stress lines at the Type I, Type II and Type VII orientation angles, it was observed that there was no regular stress distribution at the other orientation angles. It was seen that the maximum values were reached in the middle sections, while it was minimum in the ends of overlap. But this situation seems to be different in Type III, Type IV, Type V and Type VI. Specially, effect of Type IV angle was more different. It could be stated that the angles are influential both across the edge and width in the overlap region.
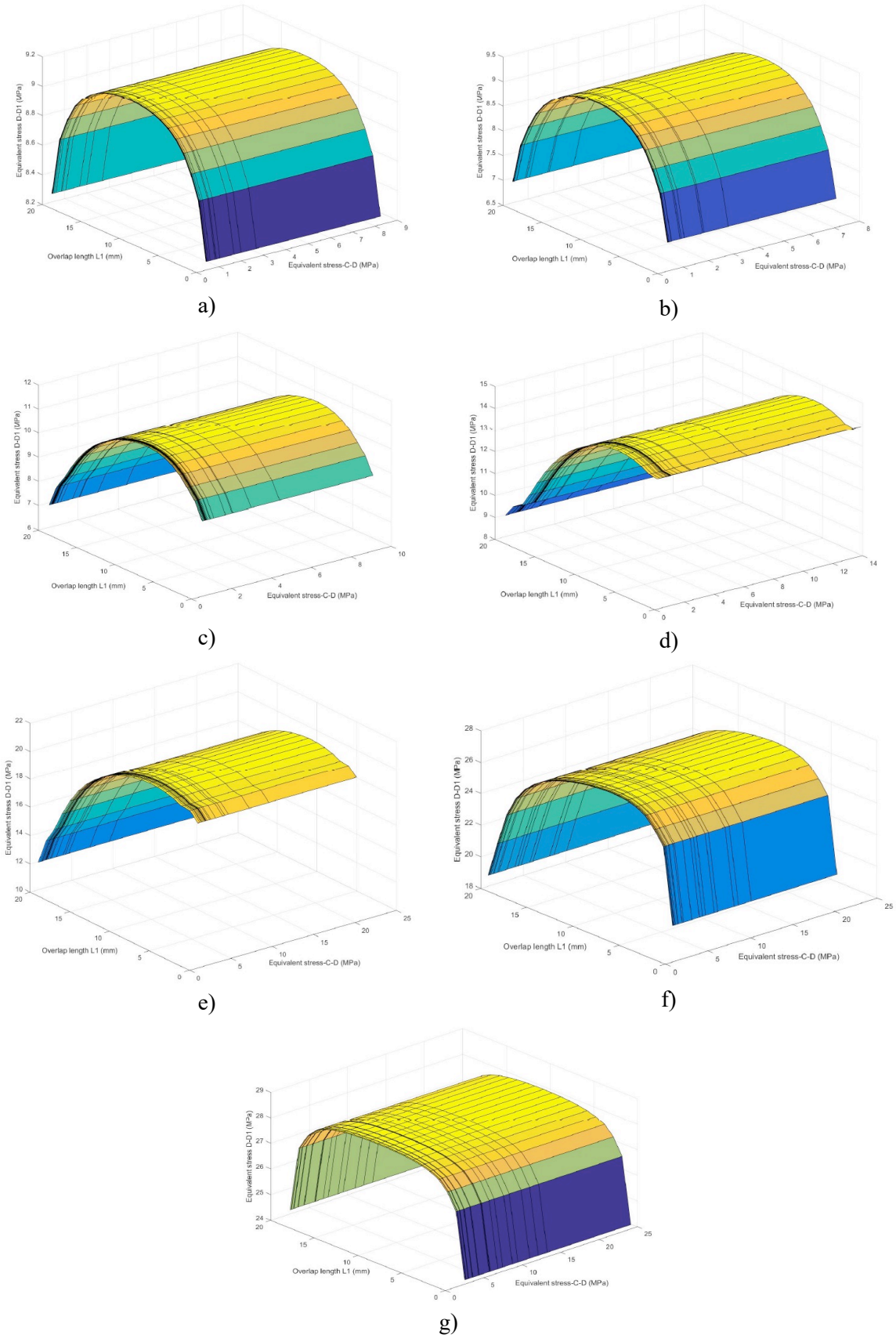
Fig. 7.The equivalent stresses compared throughout C-D and D-D1 for 20 mm on adhesive layer, a) Type I, b) Type II, c) Type III, d) Type IV, e) Type V, f) Type VI, g) Type VII
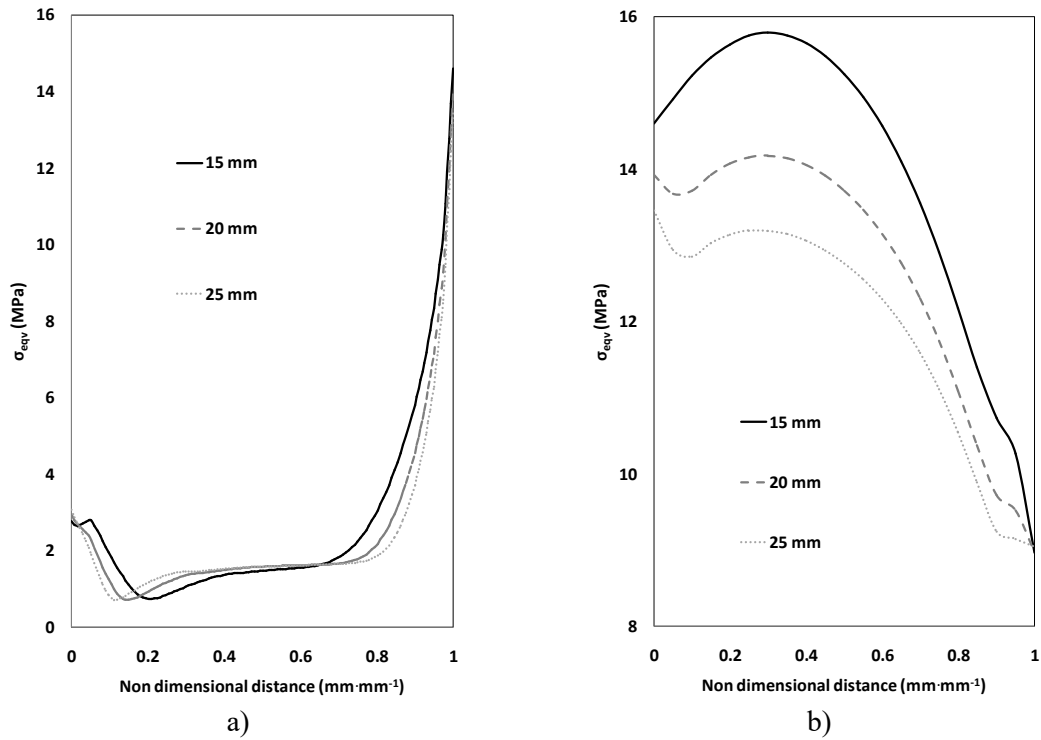
Fig. 8. Comparison the equivalent stresses for different line length (Fig. 1) considering Type IV, a) On edges, b) On width

In Figs. 8a and 8b, σ_{eqv} distributions on adhesive layer were investigated for all overlap dimensional with Type IV. On the edge, it could be stated that σ_{eqv} stresses distribution for all L1 lengths was very close. Otherwise, σ_{eqv} distributions for all overlap on width were different. σ_{eqv} distributions over the widths were listed from maximum to minimum as 15 mm, 20 mm and 25 mm, respectively. As a result, it could be said that different σ_{eqv} distributions were observed at different width lengths. Therefore, it could be said that overlap σ dimensional was important for joining.

c)
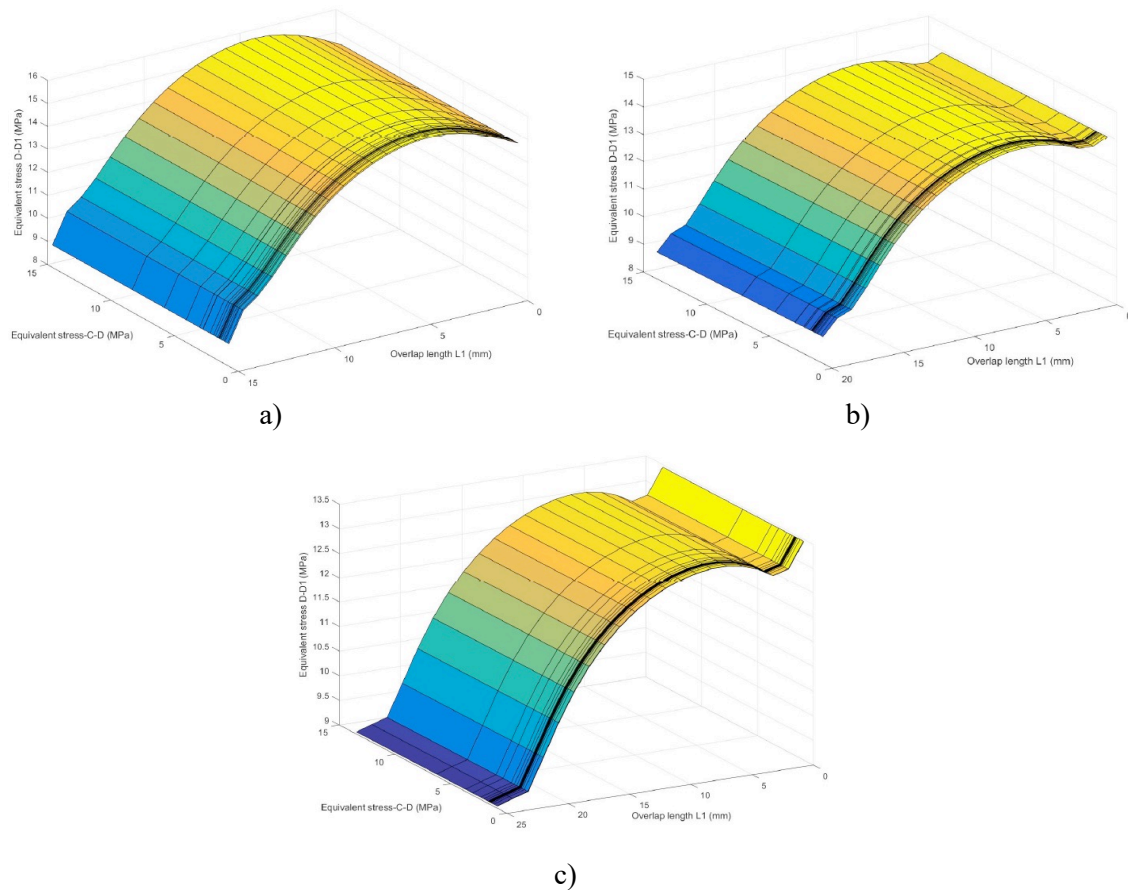
Fig. 9. Comparison the equivalent stresses for C-D and D-D1 considering Type IV, a) for 15 mm, b) for 20 mm, c) for 25 mm

As shown in Fig. 9, the equivalent stresses on C-D and D-D1 were investigated for different overlap dimensional and Type IV orientation angle. Stress values in C-D and D-D1 stress lines for each overlap dimensional were compared together on the single graph. It could be said that as the overlap length increases, differences in stress distributions occur. The greatest change was observed at 25 mm overlap dimensional.

3.2. Actions on failure load of L1 length and angles

The damage conditions of composites adhesively bonded with intermediated materials and SLJ for different parameters were presented Table 4. In Fig. 2, σ-ε behavior for adhesive was presented. In order to predict the damage load of the adhesive, the ultimate strain the (ε^*) in Table 1 was considered. The equivalent strain (ε_{eqv}) and the equivalent stress (σ_{eqv}) were computed by the von Misses yield criterion and it was assumed that the damage occurred when ε_{eqv} calculated reached the ultimate strain at any point of the adhesive layers. Also, for composites, damage control of composite parts and intermediate materials was carried out by Tsai-wu fracture criterion, taking into account the maximum strength values given in Table 2. A solution with nonlinear material behavior in the finite element analysis was reached by applying the load step by step to follow the equilibrium paths and iterating to a convergent solution with each load increase. Therefore, a pressure of 0.4 N/mm^2 per mm^2 area was for each load step. The remaining load was then applied in the last step [18-22, 24, 25].

Behaviors of σ_x, σ_y, σ_z, σ_{xy}, σ_{xz}, σ_{yz} and σ_{eqv} were generated considering tensile failure load on critical stress lines. The stresses in the interfaces of joint area were shown in Figs. 4a and 4b, the

biggest stresses on the bond-lines occur for C-D and D-D1. For that reason, stresses on these lines were investigated during the research.
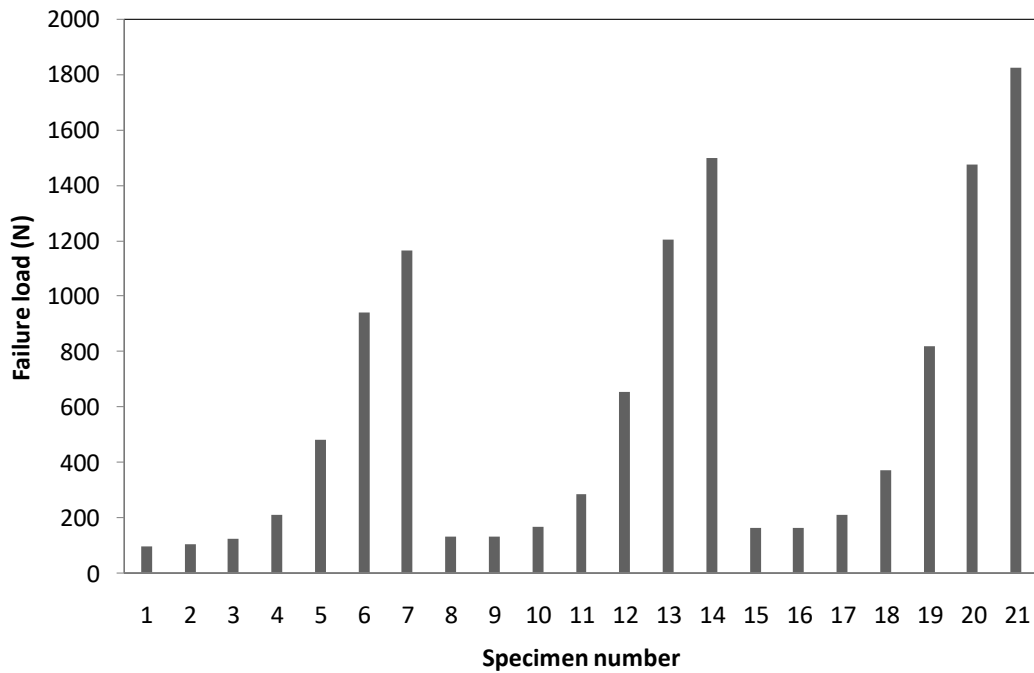
Fig. 10. The failure loads compared for all parameters

Table 4. The numerical results for joint

Specimen number	L1 (mm)	Orientation angle (^{0})	Failure load (N)
1		Type I	96.0
2		Type II	100.8
3		Type III	120.0
4	15	Type IV	206.4
5		Type V	480.0
6		Type VI	940.8
7		Type VII	1161.6
8		Type I	128.0
9		Type II	128.0
10		Type III	166.4
11	20	Type IV	281.6
12		Type V	652.8
13		Type VI	1203.2
14		Type VII	1497.6
15		Type I	160.0
16		Type II	160.0
17		Type III	208.0
18	25	Type IV	368.0
19		Type V	816.0
20		Type VI	1472.0
21		Type VII	1824.0

As presented in Fig. 10 and Table 4, the failure load of the joint with 25 mm L1 length and Type VII orientation angle were bigger than other. Also, the minimum predicted damage loads of joining with SLJ and intermediated material were Type I, Type II orientation angles. Moreover, the highest failure loads of the joint with SLJ and intermediated material were Type VII for all overlap lengths.

For 15 mm, 20 mm and 25 mm overlap dimensional; effects of angles were seen to be different in Table 4. Because failure regions were on composite part for all parameters and joint dimensional was different for each overlap length. Consequently, the highest damage loads were obtained in Type VII orientation angles, the smallest damage loads were obtained in Type I. Moreover, the largest damage load was obtained, since the joint area with 25 mm for L1 had the widest bond surface.

4. Conclusions

In the research, composite jointed with intermediated material were researched by FEM. The conclusions were as follows:

- The C-D on edges and the D-D1 on width were considered as critical stress lines for joint with SLJ and intermediated material.

- For joint with SLJ and intermediated material, σ_x, σ_y, σ_z, σ_{xy} and σ_{eqv} on critical line of adhesive layer was the highest at Type VII orientation angle.

- The σ_{yz} was the highest on critical line of adhesive layer was the highest at Type V orientation angle.

- The σ_{xz} was the highest on critical line of adhesive layer was the highest at Type VI orientation angle.

- When the stresses on C-D and D-D1 were compared together, the highest stress values occurred in Type VII.

- On the edge, the equivalent stresses for all L1 lengths were very similar.

- The equivalent stresses on width were maximum for 15 mm.

- When C-D and D-D1 stress lines were compared together for all overlap dimensional, the highest stress values occurred in 25 mm dimensional.

- The failure load of the joint with 25 mm L1 length and Type VII orientation angle were bigger than other.

- The highest failure loads were joint with Type VII for all overlap lengths.

- The smallest damage loads were obtained in Type I orientation angle.

References

[1] Xia, M., Takayanagi, H., Kemmochi, K., Analysis of multi-layered filament-wound composite pipes under internal pressure. *Composite Structures*,53, 483-491, 2001.

[2] Sulu, Ismail Yasin , Semsettin, Temiz, Failure and stress analysis of internal pressurized composite pipes joined with sleeves.*Journal Adhesion Science and Technology*, 32 (8), 816-832, 2018.

[3] Quan, Dong, Alderliesten, René,Dransfeld, Clemens,Tsakoniatis, Ioannis,Benedictus, Rinze, Co-cure joining of epoxy composites with rapidly UV-irradiated PEEK and PPS composites to achieve high structural integrity.*Composite Structures*, 251, 112595, 2020

[4] Nguyen, Tuan Hung, Grognec, Philippe Le, Analytical and numerical simplified modeling of a single-lap joint.*International Journal of Adhesion and Adhesives*, 108,102827, 2021.

[5] Sulu, Ismail Yasin , Temiz, Semsettin,Mechanical characterization of composite pipe systems joined using different radii pipes subject to internal pressure.*Mechanics Based Design of Structures and Machines*, 51(1), 566-582, 2023.

[6] Sun, Guangyong,Wei, Yang,Huo, Xintao,Luo, Quantian,Li, Qing, On quasi-static large deflection of single lap joints under transverse loading.*Thin-Walled Structures,* 170, 108572, 2022.

[7] Ma, Guoliang,Wu, Jiayu,Yuan, Hong, Interfacial shear stress analysis in single-lap adhesive joints with similar and dissimilar adherends under dynamic loading.*International Journal of Adhesion and Adhesives,* 111, 102953, 2021.

[8] Zou, Tianchun,Fu, Ji,Qin, Jiaxu,Li, Longhui,Liu, Zhihao, Failure analysis of composite-to-titanium single lap adhesive joints subjected to tensile loading.*Engineering Failure Analysis,* 129, 105734, 2021.

[9] Shang, X.,Marques, E. A. S.,Carbas, R. J. C.,Barbosa, A. Q.,Jiang, D.,da Silva, L. F. M.,D., Chen,Ju, S., Fracture mechanism of adhesive single-lap joints with composite adherends under quasi-static tension.*Composite Structures*, 251, 112639, 2020.

[10] Sahin, Resul , Akpinar, Salih, The effects of adherend thickness on the fatigue strength of adhesively bonded single-lap joints.*International Journal of Adhesion and Adhesives*, 107, 102845, 2021.

[11] Huang, Wei, Sun, Lingyu,Liu, Yang,Chu, Yantao,Wang, Jinxi, Effects of low-energy impact at different temperatures on residual properties of adhesively bonded single-lap joints with composites substrates.*Composite Structures,*267, 113860, 2021.

[12] Shi, Jia-Wei,Cao, Wen-Hai,Chen, Lei,Li, Ang-Lin, Durability of wet lay-up BFRP single-lap joints subjected to freeze–thaw cycling.*Construction and Building Materials,* 238, 117664, 2020.

[13] Lee, H. K.,Pyo, S. H.,Kim, B. R., On joint strengths, peel stresses and failure modes in adhesively bonded double-strap and supported single-lap GFRP joints.*Composite Structures*, 87, 44–54, 2009.

[14] Akhavan-Safar, A., Ayatollahi, M. R.,da Silva, L. F. M., Strength prediction of adhesively bonded single lap joints with different bondline thicknesses: A critical longitudinal strain approach.*International Journal of Solids and Structures*, 109, 189–198, 2017.

[15] Abdi, H.,Papadopoulos, J.,Nayeb-Hashemi, H.,Vaziri, A., Enhanced elastic-foundation analysis of balanced single lap adhesive joints.*International Journal of Adhesion & Adhesives*, 72, 80 – 91, 2017.

[16] Stein, N.,Mardani, H.,Becker, W., An efficient analysis model for functionally graded adhesive single lap joints.*International Journal of Adhesion & Adhesives*, 70, 117 – 125, 2016.

[17] Guin,W. E.,Wang, J., Theoretical model of adhesively bonded single lap joints with functionally graded adherents.*Engineering Structures*, 124, 316 – 332, 2016.

[18] Sülü,İsmail Yasin,Mechanical behavior of single-lap and double-lap adhesive joined composite parts.*Materials Testing*, 59(11-12), 1019-1026, 2017.

[19]Sülü, İsmail Yasin, Mechanical testing and analysis of composite parts adhesively joined under tensile load.*Materials Testing*, 59(5), 459-465, 2017.

[20] Sülü,İsmail Yasin,Temiz,Şemsettin, Mechanical behavior of composite parts joined through different processes.*Materials Testing*, 63, 411-419, 2021.

[21]Sülü,İsmail Yasin,Mechanical behavior of internal pressurized composite pipes jointed with embedded tubular sleeves.*Materials Testing*, 59(3),272-277, 2017.

[22] Sulu,İ. Y.,Temiz, Ş.,Aydin, M. D., Layer effects of multi-layered face to face adhesively bonded composite pipes subjected to internal pressure.*Academic Journal of Science*, 04(3), 195-202, 2015.

[23] Wang,B.,Xiong, J.,Wang, X.,Ma, L.,Zhang, G. Q.,Wu, L. Z.,Feng, J. C., Energy absorption efficiency of carbon fiber reinforced polymer laminates under high velocity impact.*Materials and Design,* 50, 140–148, 2013.

[24] Salih,A.,Aydin,M. D., 3-D non-linear stress analysis on the adhesively bonded composite joint under bending moment.*International Journal of Mechanical Sciences*, 81, 149-157,2014.

[25] Ozel, A.,Yazici, B.,Akpinar, S.,Aydin, M. D.,Temiz,Ş., A study on the strength of adhesively bonded joints with different adherends.*Composites Part B: Engineering*, 62, 167 – 174, 2014.

Effects of Coating Aggregates on Dynamic Properties of Concrete by Impact Resonance Method

Yisihak Gebre [a], Tom Lahmer [b], Matthias Müller [c], Abrham Gebre [d], Esayas Gebreyouhannes [e]*

[a, b] *Bauhaus-Universität Weimar, Institute of Structural Mechanics, Germany*
[c] *Bauhaus-Universität Weimar, Institute for Building Materials Science, Germany*
[a,d,e] *Addis Ababa University, Addis Ababa Institute of Technology, Ethiopia*

✉: yisihakgebre@aait.edu.et , ⓘD: *0009-0009-4127-4896 [a*], 0000-0002-1251-7301 [b], 0000-0002-0348-1570 [c], 0000-0003-0172-2905 [d], 0000-0001-9949-4597 [e]*

Abstract

Concrete structures may be subjected to dynamic loadings like earthquakes, impact, and vehicular loads. These loads may cause considerable damage to infrastructures and shorten their life span. To reduce the effects, improving concrete's dynamic properties is important. This can be done using granular elastic components and fibers in the production of concrete. This research explores the influence of using coated aggregates on the physical, mechanical, and dynamic properties of concrete. Experimental investigation on concrete with epoxy, epoxy-sand, and epoxy-crumb rubber as a partial replacement of coarse aggregates at different volume fractions ranging from 5% to 20% was conducted. Furthermore, the dynamic modulus of elasticity of concrete with coated aggregate was determined by measuring the resonant frequencies of flexural vibrations in a prismatic beam using an impactor (hammer). Results indicate that partial replacement of epoxy-crumb rubber coated aggregates in concrete shows a reduction in mechanical propriations. However, significant improvements in the mechanical and dynamic properties of concrete were observed by the partial replacement of coarse aggregates with epoxy and epoxy-sand coated aggregates. Compressive strength and dynamic elastic modulus were enhanced by 12% and 10%, respectively, when concrete with 15% epoxy-sand coated was used. The results showed that concrete specimens using epoxy and epoxy-sand coated as a partial replacement for coarse aggregate have higher mechanical properties as compared to those of concrete specimens with epoxy-crumb rubber-coated aggregates. Moreover, the results showed that the calculated values of the dynamic modulus using the empirical relations proposed by Popovics and Hansen were overestimated as compared to the experimental values.

Keywords: epoxy-sand coated, epoxy-crumb rubber coated, resonant frequencies, flexural vibrations, dynamic modulus

1. Introduction

As concrete is one of the most commonly used materials in the construction industry, it is critical to investigate its mechanical and dynamic properties. The vast application of concrete in the construction industry has led to increasing demand for improved performance against impact and dynamic loads. Several energy-absorbing materials were added to improve the ordinary concrete resistance to impact or dynamic loads and significant development has been achieved in this area [1]. Using coated aggregates is one of the recent interventions that may potentially affect; the interface bond between coarse aggregates and the matrix, the local dynamic response at the interfacial transition zone, moisture interaction between coarse aggregates and the matrix, etc. Coating of aggregates with different mixed solutions and their influence to the aggregate's properties and the properties of concrete was explored in this study.

An aggregate particle's shape can be expressed by three independent properties: form, angularity, and surface texture. The shape reflects variations in a particle's proportion and the angularity

reflects variations at the corners. Surface texture describes the irregularity of the surface at a scale too small to affect the overall shape or angularity. The three properties can be distinguished based on their various particle size scales. These characteristics are distinct from one another, which means that any one of them may change significantly without having an effect on the other two [2]. Therefore, improving the surface texture of aggregate particle's has effects on properties of concrete. The improvements are utilized by means of coating aggregates with geopolymer [3], epoxy and polymers [4], palm oil clinker powder (POCP) [5], clay [6,7], plastics [8-13], silicon [14], hydrophobic polymers and styrene-butadiene rubber (SBR) [15], and other nanoparticles.

Geopolymer coating of lightweight aggregates (LWA) has been investigated by Shahedan, N. F., et al., [3] and it has been proven to enhance the properties of lightweight aggregate. The coating of aggregate can decrease the water absorption, excellent durability and bonding strength. Geopolymer coatings are sustainable materials because of their low pollution, and environmental friendliness, as well as their superior performance. Lim, Taekyung, et al., [4] observed high-strength functional lightweight aggregates using epoxy-TiO_2 coating. They also indicated the strength properties of the LWA are dependent on the concentration of epoxy and coating method. Abutaha, F., et. al, [5], investigated the mechanical properties of palm oil clinker (POC) concrete using palm oil clinker powder to fill up and coat the surface voids of POC coarse aggregate under different (0-100%) replacement of coarse aggregates. By providing enough paste to coat the POC surface voids, POCP coating greatly improved the compressive strength of the POC concrete [5].

Clay-coated coarse aggregates were observed to cause higher values of drying shrinkage in concrete and adding extra water did not result in significant increases in its shrinkage property at later ages [6]. Moreover, a study conducted by [7] identified the effects of clay coating on concrete properties. The researchers selected four clay types: sodium montmorillonite (NaM), calcium montmorillonite (CaM), kaolin and illite to coat the coarse aggregate. Based on their findings, the compressive strength of clay-coated aggregates with NaM and CaM clays was significantly lower than that of the control mix by approximately 88% and 75%, respectively. Additionally, these two clay coatings also reduced the split tensile strength by 80% and 65%, respectively. However, kaolin and illite coatings essentially have no effect on compressive strength of concrete.

Plastic wastes such as Polyethylene (PE), Polypropylene (PP) and Polystyrene (PS) by mixing with various types of hot bitumen were also used for coating coarse aggregates in concrete [8-13]. Generally, these types of coating are described as Plastics Coated Aggregate (PCA).

PCA at a higher percentage (up to 25%) were found to improve adhesion property and aggregate strength [8]. Experimental investigation, on partially replaced coarse aggregates with coated aggregates with polypropylene waste plastic resulted in reductions in crushing strength (by 5.09%), impact strength (by 1.67%) and abrasion resistance (by 8.27%) as compared to uncoated coarse aggregates [9]. A separate study on PCA was observed to enhance binding capacity, Marshall stability, strength, and load bearing capacity for road construction application. In addition, the abrasion resistance and impact strength were improved when PCA was used [10-12]. Interestingly, their technology not only strengthened road construction, but also increased road life with reduced environmental impact.

According to Dawale, S. A. [13], plastic wastes (e.g., discarded carry bags, films, and cups) were used to coat coarse aggregates with bitumen. From the study, results indicated that there were improvements in properties such as water absorption, stripping value, and soundness. The PCA mixture has a lower penetration value and a higher softening point, as well as adequate ductility.

The study conducted by [14] investigated the effect of silicon coated aggregates on concrete properties. In the study, mechanical properties of concrete were investigated under different loading rates. Results revealed that, the compressive strength with silicon coated aggregates with 5% replacement level had slightly increased. However, for 10% and 15% silicon coatings, the compressive strength was reduced in all loading rates. In addition, a higher reduction in static modulus of elasticity (30% - 43.5%) was exhibited.

Furthermore, the study [15] investigated the effect of coating of scoria and Leca aggregates using hydrophobic polymers-polyvinyl acetate (PVA) and styrene-butadiene rubber (SBR) polymers on the mechanical and microstructural properties of lightweight concrete. Coatings were applied in single and double layers. Test results showed that, the compressive strength of mixtures containing scoria lightweight (coated with one or two layers) increased by 21%. Moreover, the compressive strength for mixes containing Leca lightweight aggregates increased by 13.5%.

The focus of the previous researches discussed above is mainly on non-dynamic properties of concrete with coated aggregates. In this study, the effect of coating aggregates with epoxy, epoxy-sand and epoxy- crumb rubber on the mechanical as well as the dynamic properties of concrete were experimentally investigated. The dynamic modulus of elasticity as determined by the impact resonance method is compared with the theoretical results obtained from the static modulus using the relation proposed by Popovics [16]. Moreover, the dynamic modulus is compared with the results determined from the compressive strength using the relationship developed by Hansen [17].

2. Materials, Mix Design, and Experimental Program

2.1. Material Characterization

For the preparation of concrete mixtures, Portland OPC 42.5 grade cement, sand and crushed stone with a maximum size of 25 mm were used. In this study, to coat aggregates, Sika -161 and T 19 - 32/1000 epoxy resins were used. Furthermore, crumb rubber particle sizes ranging from 2.5-3.5 mm and standard sand particle sizes ranging from 0.75-2.0 mm are used for coating aggregates. Table 1 shows the physical properties of standard sand, crumb rubber, sand and coarse aggregates. The gradation requirements of sand and coarse aggregates were checked and both aggregates satisfy the requirement set on ASTM C 136 [18]. Properties of epoxy resin (Sika - 161 and Epilox T 19-32/1000) and Polymeric coupling agent (BYK-C 8001) are presented in Table 2.

Table 1. Physical properties of standard sand, sand, coarse aggregates and rubber

Physical properties	Standard sand	Sand	Coarse aggregate	Crumb rubber
Specific gravity	2.6	2.5	2.7	1.03
Moisture content %	< 0.2	2.4	1.3	
Water absorption %	0.7	2.04	1.02	
Unit weight kg/m³	1580	1405	1615	720

Concrete specimens of various sizes were cast and tested. Tests were carried out in accordance with EN (European Norm) and ASTM (American Society for Testing and Materials) standards. Concrete mixtures with replacement of maximum 20% coarse aggregate by epoxy, epoxy - sand and epoxy- crumb rubber coated aggregates with an increment of 5% are considered.

Table 2. Properties of Epoxy resins and Coupling Agent

Sika -161 Epoxy [19]	Epilox® T 19-32/1000 [20]	Coupling Agent BYK-C 8001 [21]
density approx. 1.65 g/cm³ (23 °C) Shore D Hardness ~76 (7 days / +23 °C) (DIN 53 505) Compressive Strength > 45 N/mm² (mortar screed, 28 days / +23 °C / 50 % r.h.) (EN13892-2)	density approx. 1.14 g/cm³ (20 °C) liquid, solvent-free, crystallization-inhibited, low-molecular and low viscosity epoxy resin viscosity at 25 °C (1.0-1.3 (Pa·s))	density 1.035 g/cm³ (20 °C) melting point/range < -76 °F (< -60 °C) initial boiling point 194 °C (1,013 hPa) vapor pressure ca. 0.55 hPa (20 °C) Viscosity, dynamic 34 mPa.s (68 °F (20 °C))

The control mix is designated as CM-0, concrete with epoxy coated aggregates as ECA-n, with sand coated aggregates as SCA-n and with crumb rubber coated aggregates as RCA-n. The letter n indicates the replacement level (e.g., ECA-15 represents concrete with 15% replacement of coarse aggregate by epoxy-coated aggregates).

2.2. Mix Design

The proportion of materials is determined using a volume-based mix design method. Concrete mixtures incorporating coated aggregates with epoxy, epoxy-sand and epoxy-crumb rubber at 0%, 5%, 10%, 15% and 20% substitution of coarse aggregate were prepared. Cement, sand and coarse aggregate mix proportion of 1:1.5:3 was used, with a water-cement ratio for all mixtures was 0.45.

Manual coating is used for each of the coatings used in the study. For the epoxy coated aggregates, the aggregates are only coated with epoxy. For the epoxy-sand and epoxy-crumb rubber coated aggregates, initially the aggregates are coated with epoxy and are left for 45-60 min. The epoxy coated aggregates, and then thoroughly blended with the standard sand for the epoxy-sand coated aggregates and with crumb rubber for the epoxy-crumb rubber coated aggregates. During this process, the sand and crumb rubber stick on the surface of the epoxy coated aggregates (see Figs. 2b and 2c). Finally, the coated aggregates are allowed to dry for three days (under a temperature T = 20ºC and relative humidity RH=70%) before being used to make concrete mixtures. It can be observed that the sand and crumb rubber particles are well distributed over the surface of the aggregates, see Figs. 2b and 2c.

Fig 1 shows samples of crumb rubber and standard sand used in this study for coating the natural coarse aggregates. Moreover, samples of coated aggregates with epoxy, epoxy-sand, and epoxy-crumb rubber are shown in Fig 2.

<table>
<tr><td>(a)   crumb rubber</td><td>(b)   standard sand</td></tr>
</table>

Fig. 1. Crumb rubber and standard sand samples
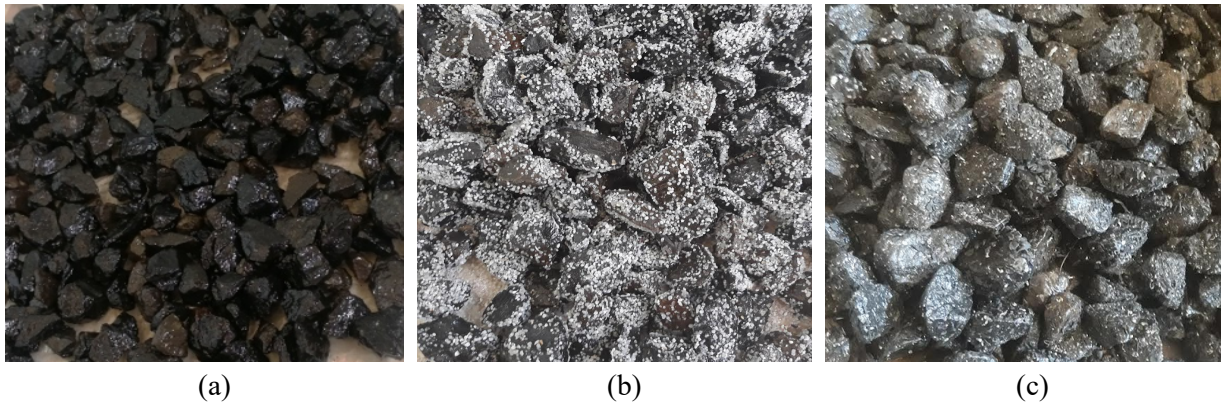
(a)   (b)   (c)

Fig. 2. (a) epoxy coated   (b) epoxy-sand coated   (c) epoxy-crumb rubber coated aggregates

2.3. Experimental Program

2.3.1. Test Methods

Testing procedures for measuring the mechanical and dynamic properties of concrete, such as compressive strength, split tensile strength, static and dynamic moduli of elasticity of concrete are conducted in accordance with ASTM and EN test standards and tests are carried out on 28th days aged concrete specimens.

Compressive strength test (cube specimens with 150 mm dimensions) is conducted following EN 12390-4: 2019 testing procedure [22]. For split tensile strength test (cylindrical specimens with dimensions of 300 mm in length and 150 mm diameter), ASTM C496-96 [23] and EN 12390-6 [24] test procedures were performed. The static modulus of elasticity (cylindrical specimens with dimensions of 300 mm in length and 150 mm diameter) is determined as per EN 12390-13:2021[25] standard. Moreover, for dynamic modulus of elasticity test (beam specimen with 100mm×100mm×500mm), impact resonance testing was performed as per ASTM C215-08 standard [26].

2.3.2. Fundamental Transverse Resonant Frequencies

In the experimental program, using the Impact Resonance Testing (IRT), the fundamental transverse resonant frequency of concrete specimens was measured and the corresponding dynamic modulus of elasticity of concrete is calculated. For transverse vibration, the support nodes are located at a distance equal to 0.224 times the length of the specimen (L) away from the ends of the specimen. The schematic diagram of a test setup for a rectangular concrete prism with square dimensions of 100 mm and a length of 500 mm is shown in Fig. 3.
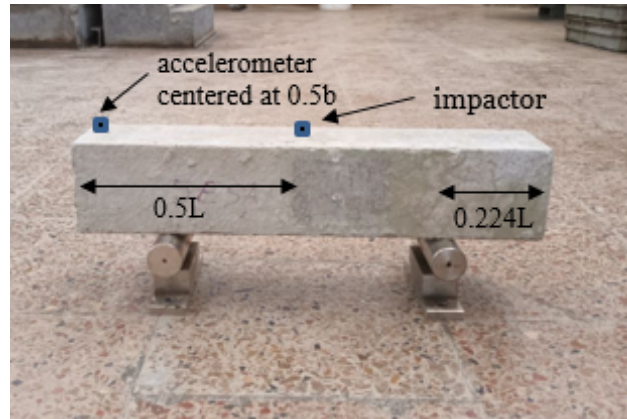
Fig. 3. Schematic of transverse mode (ASTM C215-08)

A hammer (small impactor of 750 gm), an accelerometer (Arduino type, MPU-6050) and a computer are used to test the impact resonance frequency. The impact point was at the mid span of the prism's top face, and the accelerometer was attached to the specimen's positioned 20 mm from the edge. The locations of the accelerometer, impact point, and boundary conditions remained consistent across all concrete specimens. To allow free vibration in the fundamental transverse mode with a free-free boundary condition, the supports are placed at nodal points. The instrumentation and experimental test setup employed in this study is shown in Fig. 4.

Fig. 4. Experimental Test set-up: accelerometer (Arduino type, MPU-6050) and impactor

2.3.3. Determination of Resonant Frequencies

Under free-free boundary conditions, a supported prismatic beam specimen is struck manually with an impact hammer to produce vibration. The Arduino UNO board was connected to a computer via Arduino software to record time domain signal of the specimen response received from the accelerometer and then transformed the recorded time domain signal into amplitude-frequency domain using MATLAB code based on Fast Fourier Transform (FFT). The resonant

frequency (frequency corresponding to the peak amplitude) is then determined from the Frequency Response Function (FRF).

2.3.4. Dynamic Modulus of Elasticity

In this section, IRT method, which is a dynamic young's modulus measurement technique, is briefly described. According to ASTM C215-08, the dynamic modulus of elasticity of concrete, E_d, is calculated from the fundamental transverse frequency, mass, and dimensions of the test specimen. For the prismatic specimen, the dynamic modulus of elasticity (E_d) can be given by the following Eq. (1) [26]:

$$E_d = 0.9464 Mn^2 T\left(\frac{L^3}{bt^3}\right) \tag{1}$$

where E_d is the dynamic modulus of elasticity (Pa), M is the mass of prism (kg), n is the fundamental transverse resonant frequency (Hz), L is the prism Length (m), b, t are the cross-sectional dimensions of the prism (m), and T is the correction factor.

The correction factor depends on the ratio of the radius of gyration, K, (for a prism K = t/3.464), the length of the specimen (L) and the Poisson's ratio. Numerical values of the correction factor for various values of Poisson's ratio and K/L are given in ASTM C215-08 [26].

3. Results and Discussions

The mechanical and dynamic properties of conventional concrete and concrete with coated aggregates (epoxy resin, epoxy-sand and epoxy-crumb rubber coated) were tested and results are presented in the following subsections.

3.1. Mechanical Properties

Test results on the compressive strength, split tensile strength, and static modulus of elasticity of concrete with various coating fractions are presented in Table 3 below. Three tests were conducted on each sample, and average values are presented. Additionally, graphs of the test results are shown in Figs. 5-7.

Table 3. Compressive, split tensile strength and static modulus of elasticity of concrete

| Percentage replacement (%)	Compressive strength (MPa)			Split tensile strength (MPa)			Static Modulus (GPa)		
	Epoxy coated	Sand coated	rubber coated	Epoxy coated	Sand coated	rubber coated	Epoxy coated	Sand coated	rubber coated
0	37.79	37.79	37.79	2.37	2.37	2.37	29.98	29.98	29.98
5	38.77	40.81	37.42	2.43	2.38	2.24	30.68	31.16	29.54
10	37.28	41.03	36.64	2.25	2.49	2.16	27.70	29.68	28.05
15	34.59	42.41	34.97	2.28	2.43	2.12	27.25	28.59	27.40
20	33.46	41.17	34.11	2.16	2.30	2.08	28.22	29.73	25.64
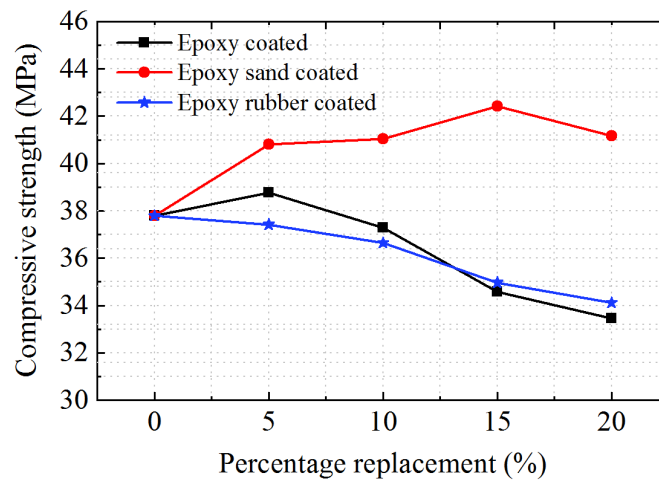
Fig. 5. Compressive strength (MPa)

Based on the test results shown in Table 3, the compressive strength of concrete with coated aggregates was in the range between 34.1 and 42.4 MPa. Optimal compressive strength of concrete was observed for SCA-15, which is an increment of 12%. The increment was observed due to the formation of rough texture of the surface when the aggregates were coated with epoxy-sand, which enhances the bond between the matrix and the aggregate surface. However, the maximum reduction in compressive strength was at ECA-20, i.e., approximately 11% lost with respect to the control mix. The strength reduction may be caused due to weak interface strength between the epoxy coated aggregates and the matrix.

For epoxy coated aggregates, a slight increment of 3% was noticed in its compressive strength at 5% replacement level. This is due to the presence of smaller, locally formed micro-cracks that changes the crack patterns at this localized area. According to a study in [27], the presence of primary micro-cracks did not affect the compressive strength of concrete, but remarkable reduction was observed as the crack width and crack angle increased. However, beyond 5% replacement level of epoxy-coated aggregates, a reduction in compressive strength ranging from 2% to 11% was observed. The reduction is caused by the development of smooth texture which decreases the contact area. This results a poor bond between the interface of aggregate and the matrix. For RCA-5, there is a slight reduction of 0.95% in compressive strength was achieved. For the other rubber coated aggregates, a reduction of 3% - 10% was observed.
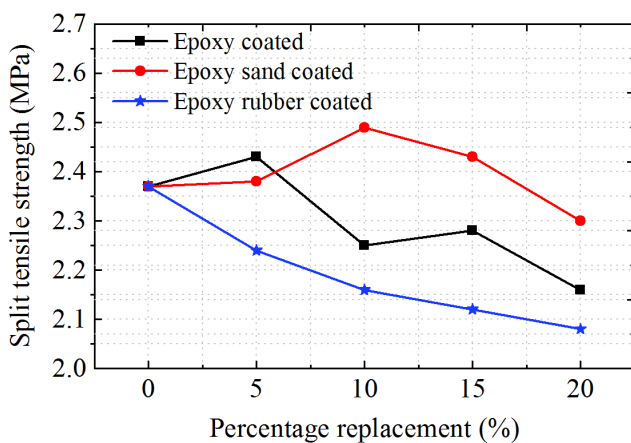
Fig. 6. Split tensile strength (MPa)
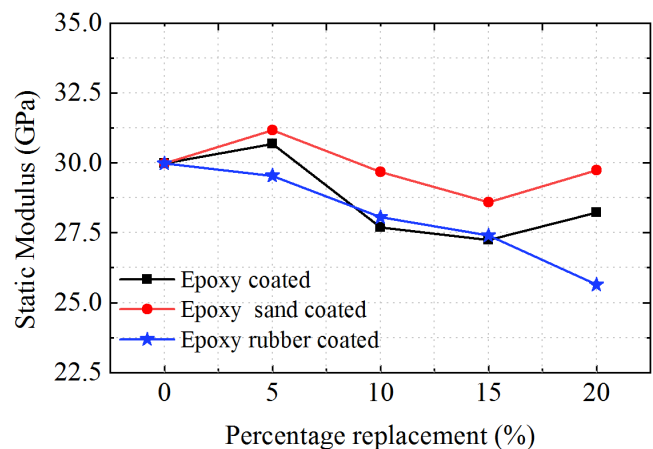
Fig. 7. Static Modulus of Elasticity (GPa)

As shown in Fig. 6, for split tensile strength, there is a higher reduction up to 12% was observed. Maximum split tensile strength is obtained when SCA-10 concrete mix was used, resulting an increment of 5%. Moreover, as shown in Fig. 7, better results in static modulus were achieved if ECA-5 and SCA-5 coatings have been used. It is also observed that, the optimal static modulus (4% increment) was achieved if SCA-5 mix was used. Unlike ordinary concrete, the increase in compressive strength is not directly associated with the increase of static modulus with partial replacement of epoxy-sand coated aggregates. It can be observed that the compressive strength of the SCA concrete increases with the replacement of coated aggregates, however the static modulus reduces with the increase in replacement of epoxy-sand coated aggregates.

3.2. Dynamic Modulus of Elasticity (Impact Resonance Method)

The dynamic modulus of elasticity was determined by using the impact resonance method for concrete with coated aggregates of different coating materials. Samples of the acceleration time history is shown in Fig. 8 below. Moreover, Fig. 9 shows the Frequency Response Function (FRF) of SCA-5 and RCA-15 concrete specimens.

(a) SCA -5

(b) RCA -15

Fig. 8. Acceleration time history

(a) SCA -5 Test 2

(b) RCA -15 Test 3
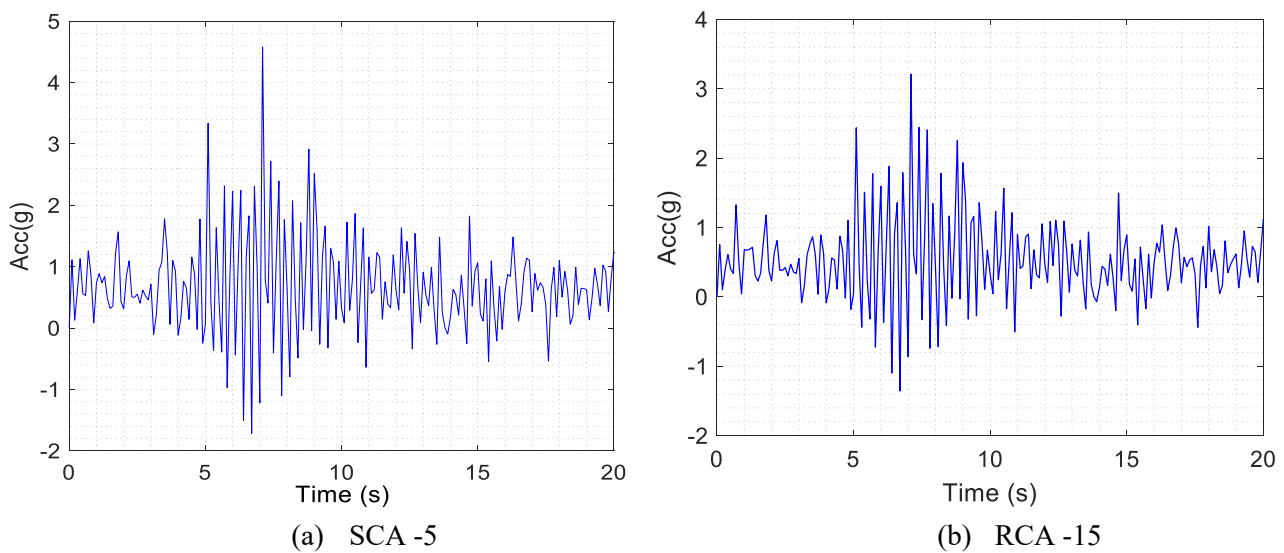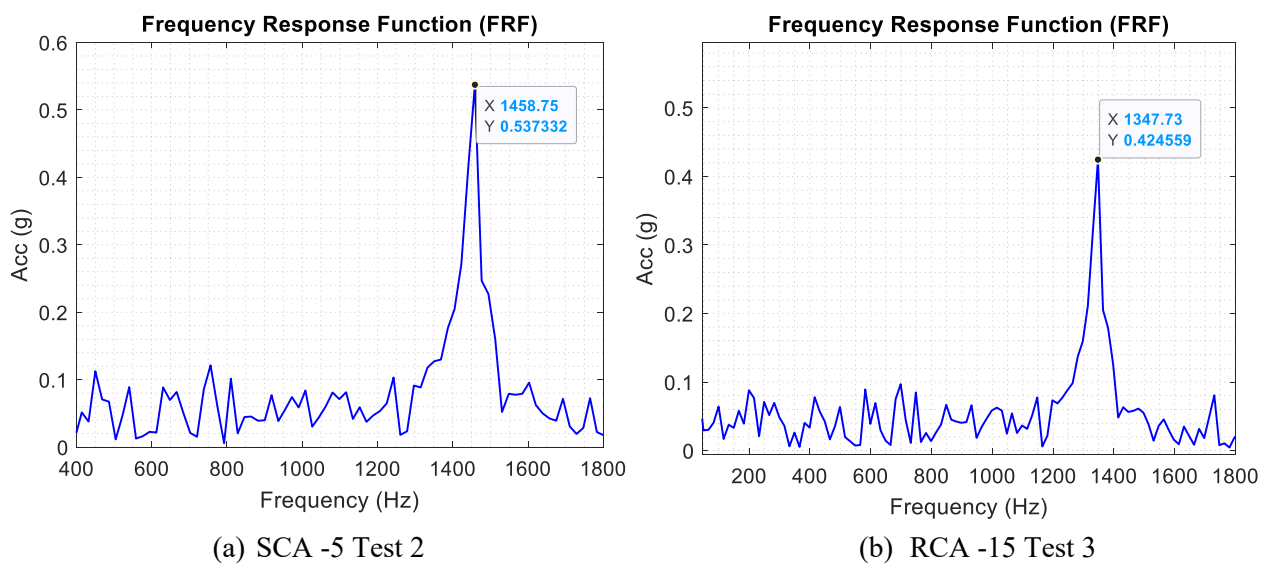
Fig. 9. Samples of Frequency Response Function (FRF)

The dynamic modulus of elasticity of concrete, E_d, is computed using Eq. (1) and the results are

presented in Table 4. For each concrete specimen, three repeated tests were performed and mean values of the resonant frequency were taken for the determination of the dynamic modulus of elasticity. For the tested specimen with a K/L ratio of 0.06 and a Poisson's ratio of 0.24, the correction factor (T) is 1.29 [26].

Table 4. Resonant Frequency and Dynamic Modulus of Elasticity

| Notation	Mass of Prism (kg)	Average values		CoV (%)	Increment (%)
		Resonant Frequency (Hz)	Dynamic Modulus (GPa)		
CM-0	10.55	1452.30	33.96	3.47	-
ECA-5	10.72	1465.00	35.11	2.13	3.39
ECA -10	10.47	1423.31	32.37	1.99	-4.68
ECA -15	10.65	1385.43	31.20	1.17	-8.13
ECA -20	10.75	1365.63	30.59	3.93	-9.92
SCA -5	10.43	1457.04	33.79	2.60	-0.49
SCA -10	10.95	1448.19	35.05	3.04	3.21
SCA -15	10.98	1490.02	37.20	2.96	9.55
SCA -20	10.95	1411.98	33.32	1.53	-1.89
RCA-5	10.17	1499.16	34.88	1.37	2.72
RCA -10	10.59	1438.86	33.46	3.48	-1.47
RCA -15	10.95	1370.06	31.37	2.88	-7.63
RCA -20	10.86	1344.67	29.97	3.29	-11.75

As shown in Table 4, an optimal dynamic modulus of elasticity is obtained with SCA-15, which resulting nearly 10% increment compared to the control mix. While, for 5% replacement of aggregates with epoxy and epoxy-crumb rubber coated aggregates, there was an increment of 3.4 % and 2.7%, respectively. For RCA-20, a maximum reduction (approximately 12%) in dynamic modulus of elasticity is observed. In general, increasing the percentage level of coated aggregates with epoxy, epoxy-sand and epoxy-crumb rubber, reduction in the dynamic modulus of elasticity was exhibited. Moreover, concrete specimens with varying percentages of coated aggregate replacement, the CoV of the dynamic modulus of elasticity ranges from 1.17% to 3.93%.

3.3. Relationship between Compressive Strength, Static and Dynamic Moduli of Concrete

Many researchers have found relationships to correlate the static and dynamic moduli of elasticity. Based on a large sample of concrete specimens, with compressive strengths ranging from 24MPa to 161MPa, Popovics developed linear empirical relations that is given in the following Eq. (2) [16].

$$E_s = 0.83 E_d \tag{2}$$

where E_s is the static modulus of elasticity (GPa) and E_d is the dynamic modulus of concrete (GPa).

According to Hansen, an empirical relationship for concrete's dynamic modulus of elasticity and compressive strength is developed and given by the following expression [17].

$$E_d = 5.31 f_c^{0.5} + 5.83 \tag{3}$$

where E_d is the dynamic modulus of elasticity of concrete (GPa) and f_c is the compressive strength of concrete (MPa).

For comparison, the dynamic modulus of elasticity of concrete obtained from experimental tests (impact resonance method) and values estimated from the empirical relations using Eqs. 2 and 3 is presented in Table 5 below.

Table 5. Dynamic Modulus of Elasticity (Experimental and predicted values)

Notation	Compressive Strength (MPa)	Static Modulus (GPa)	Dynamic Modulus (GPa)			Ratio	
			Hansen (1)	Popovics (2)	IRT method (3)	(1)/(3)	(2)/(3)
CM-0	37.79	29.98	38.47	36.12	33.96	1.13	1.06
ECA-5	38.77	30.68	38.89	36.96	35.11	1.11	1.05
ECA -10	37.28	27.70	38.25	33.37	32.37	1.18	1.03
ECA -15	34.59	27.25	37.06	32.83	31.2	1.19	1.05
ECA -20	33.46	28.22	36.55	34.01	30.59	1.19	1.11
SCA-5	40.81	31.16	39.75	37.54	33.79	1.18	1.11
SCA -10	41.03	29.68	39.84	35.76	35.05	1.14	1.02
SCA -15	42.41	28.59	40.41	34.45	37.20	1.09	0.93
SCA -20	41.17	29.73	39.90	35.82	33.32	1.20	1.08
RCA -5	37.42	29.54	38.31	35.59	34.88	1.10	1.02
RCA -10	36.64	28.05	37.97	33.81	33.46	1.13	1.01
RCA -15	34.97	27.40	37.23	33.01	31.37	1.19	1.05
RCA -20	34.11	25.64	36.84	30.89	29.97	1.23	1.03

Moreover, Figs. 7 and 8 show the dynamic modulus of elasticity of concrete determined by the impact resonance testing method (experimental values) and the predicted values obtained from the formulas proposed by Popovics and Hansen, respectively.
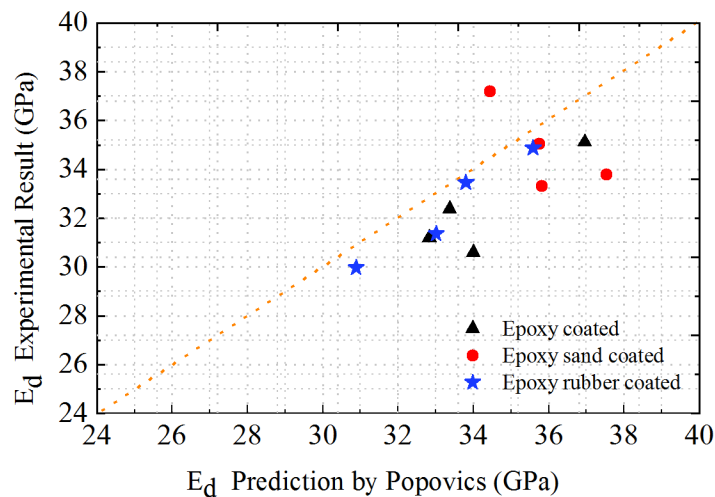

Fig. 7. Comparison of experimental and predicted values (by Popovics's formula) for the dynamic modulus of elasticity of concrete specimens
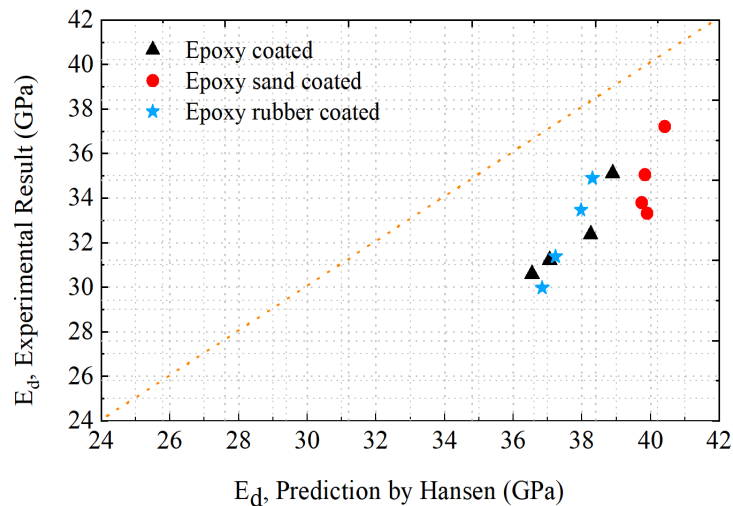
Fig. 8. Comparison of experimental and predicted values (by Hansen's formula) for the dynamic modulus of elasticity of concrete specimens

As shown in Table 5, the variation of the predicted dynamic modulus of elasticity of concrete calculated by Popovics's [16] formula to the corresponding experimental values ranges from 1.5% to 11%. Moreover, experimental measurements and the computed dynamic modulus of elasticity using Hansen's [17] formula differ by 8% to 23%. The findings showed that the dynamic modulus of elasticity obtained by measuring experimental values using the IRT method yielded a lower value than the predicted values by using the empirical relations proposed by both Popovics and Hansen. The variation is observed due to that, the relations (Eqs. 2 and 3) are developed for conventional concrete, whereas in this study the coarse aggregates were partially coated with epoxy, epoxy-sand and epoxy-crumb rubber. Thus, for concrete with coated aggregates, the suggested formula, in particular Hansen's formula, has significant differences and is not appropriate for predicting the dynamic modulus of elasticity of concrete.

4. Conclusions

The experimental processes of coating aggregates with epoxy, epoxy-sand and epoxy-crumb rubber were successfully carried out and has effects on the mechanical and dynamic properties of concrete. Based on the findings obtained from this study, coating aggregates with epoxy-sand can be used for concrete, which makes rough-textured aggregate surface and provide better interlocking and a good bond between the aggregate and the mortar mix.

Epoxy-sand coating of aggregates is found to enhance the compressive and splitting tensile strength of concrete up to a replacement of 15% of the natural coarse aggregates. Interestingly, the increase in compressive strength is not directly associated with the increase of static modulus for the concrete with partial replacement of epoxy-sand coated aggregates.

Generally, partial replacement of coarse aggregates with epoxy and epoxy-crumb rubber coated aggregates significantly reduces the mechanical properties of concrete. This reduction is due to the increase in crack width and the formation of smooth surface which weakened the interface bond strength between the coated aggregates and the matrix. However, partially replacing the coarse aggregates by epoxy and epoxy-crumb rubber coated aggregates can improve the dynamic properties of concrete.

Acknowledgement

Notations

b, t	Cross-sectional dimensions of prism
E_d	Dynamic modulus of elasticity
E_s	Static modulus of elasticity
f_c	Compressive strength of concrete
L	Prism length
M	Mass of prism
n	Fundamental transverse resonant frequency
T	Correction factor

Abbreviations

ASTM	American Society for Testing and Materials
CoV	Coefficient of variation
EN	European Norm
FFT	Fast Fourier Transform
FRF	Frequency Response Function
IRT	Impact Resonance Testing
LWA	Lightweight Aggregates
PCA	Plastics Coated Aggregate
PE	Polyethylene
POC	Palm Oil Clinker
POCP	Palm Oil Clinker Powder
PP	Polypropylene
PS	Polystyrene
PVA	Polyvinyl acetate
SBR	Styrene-Butadiene Rubber

References

[1] Lu, Song, Jin-Yu Xu, Er-Lei Bai, Xin Luo., Effect of Particles with different Mechanical Properties on the Energy Dissipation Properties of Concrete. *Construction and Building Materials,* 144, 502-515, 2017.

[2] Sakthivel, S.N., Kathuria, A., Singh, B., Utilization of Inferior Quality Aggregates in Asphalt Mixes: A Systematic Review. *Journal of Traffic and Transportation Engineering*, 9(5), 864-879, 2022.

[3] Shahedan, Noor Fifinatasha, Mohd Mustafa., Potential of Geopolymer Coating for Lightweight Aggregate via Milling and Dipping Method: A Review. *European Journal of Materials Science and Engineering,* 7(2), 094–105, 2022.

[4] Lim, T., Lee, J.H., Mun, J.H., Yang, K.H., Ju, S., Jeong, S.M., Enhancing Functionality of Epoxy–TiO$_2$-Embedded High-Strength Lightweight Aggregates. *Polymers,* 12(10), 1-11, 2020.

[5] Abutaha, F., Abdul Razak, H., Ibrahim, H.A., Effect of Coating Palm Oil Clinker Aggregate on the Engineering Properties of Normal Grade Concrete. *Coatings*, 7(10), 1-26, 2017.

[6] Muñoz Jose F., Expanded Study on the effects of Aggregate Coating and Films on Concrete Performance, *Wisconsin highway research program*, 2007.

[7] Muñoz, Jose F., M. Isabel Tejedor, Marc A. Anderson, and Steven M. Cramer., Detection of aggregate clay coatings and impacts on concrete. *ACI Materials Journal*, 107(4), 387-395, 2010.

[8] Rajasekaran, S., Vasudevan, R., Paulraj, S., Reuse of Waste Plastics Coated Aggregates-Bitumen Mix Composite for Road Application - Green Method. *American Journal of Engineering Research*, 2(11), 1-13, 2013.

[9] Alave, Y.B., Mahimkar, S.S., Patil, K.S., Gupta, J.J., Kazi, A., Experimental Investigation of Plastic Coated Aggregate. *International Journal of Engineering Research & Technology,* 9(3), 112-120, 2021.

[10] Sharma, S.D., Sharm, A., Utilization of Waste Plastic in Flexible Pavement. *International Journal of Science and Research*, 8(5), 1545-1549, 2019.

[11] Vasudevan, R.N.S.K., Nigam, S.K., Velkennedy, R., Sekar, A.R.C., Sundarakannan, B., Utilization of Waste Polymers for Flexible Pavement and Easy Disposal of Waste Polymers. *International Journal of Pavement Research and Technology,* 3, 34-42, 2010.

[12] Harnadh K.L., A. M. N. Kashyap, K. M. Gupta, Experimental Investigation on Coarse Aggregates by using Waste Plastics & Polymers. *International Journal of Innovative Resresach in Engineering and Management,* 2(3), 19-23, 2015.

[13] Dawale, S.A., Use of Waste Plastic Coated Aggregates in Bituminous Road Construction. *International Journal of Advancement in Engineering Technology, Management, and Applied Science,* 3(6), 118-126, 2016.

[14] Gebre, Y., Lahmer, T., Müller, M., Wiegand, T., Osburg, A., & Tarekegn, A. G., Properties of Concrete with Coated Aggregates under different Loading Conditions. *Journal of Research in Engineering and Applied Sciences*, 8(1), 449-459, 2023.

[15] Vahabi, Mir Yashar, Behzad Tahmouresi, Hossein Mosavi, and Siavash Fakhretaha Aval., Effect of pre-coating lightweight aggregates on the self-compacting concrete. *Structural Concrete*, 23(4), 2120-2131, 2023.

[16] Popovics, J.S., Zemajtis, J., Shkolnik, I., A Study of Static and Dynamic Modulus of Elasticity of Concrete, *American Concrete Institute - Concrete Research Council*, Report 16, 2008.

[17] Hansen, T. C., Recycled Aggregate and Recycled Aggregate Concrete. *Material and Structures,* 19, 201-246, 1986.

[18] ASTM C 136 - Standard Test Method for Sieve Analysis of Fine and Coarse Aggregates, *ASTM International*, 2014.

[19] Sikafloor®-161, Product Data Sheet, May 2019.

[20] Epoxy T 19-32/1000, Product Data Sheet, February 2019.

[21] BYK-C 8001, Polymeric Coupling Agent, Product Data Sheet, 2021.

[22] EN 12390-4:2019: Testing Hardened Concrete - Part 4: Compressive Strength of Test Specimens, 2019.

[23] ASTM C496-96: Standard Test Method for Splitting Tensile Strength of Cylindrical Concrete Specimens, *ASTM International*, 2017.

[24] EN 12390-6:2009: Testing Hardened Concrete - Part 6: Tensile Splitting Strength of Test Specimens, 2009.

[25] EN 12390-13:2021: Testing Hardened Concrete - Part 13: Determination of Secant Modulus of Elasticity in Compression, 2021.

[26] ASTM C215-08: Standard Test Method for Fundamental Transverse, Longitudinal and Torsional Resonant Frequencies of Concrete Specimens, *ASTM International*, 2009.

[27] Miura, T., Sato, K., Nakamura, H., The Role of Microcracking on the Compressive Strength and Stiffness of Cracked Concrete with different Crack Widths and Angles Evaluated by DIC. *Cement and Concrete Composites,* 114, 1-10, 2020.

Vibration Analysis of Porous Orthotropic Cylindrical Panels Resting on Elastic Foundations Based on Shear Deformation Theory

Ferruh Turan

Ondokuz Mayis University Faculty of Engineering Department of Civil Engineering

✉: ferruh.turan@omu.edu.tr , 🆔: *0000-0002-4160-712X*

Abstract

Cylindrical panels are one of the most essential structural members of engineering structures, with mechanical, civil, aeronautical, and marine engineering applications. They are subjected to a wide range of vibrational loads. This article presents a novel higher-order porosity distribution and a free vibration analysis for porous orthotropic cylindrical panels resting on elastic foundations under higher-order shear deformation theory. It is assumed that cylindrical panels are composed of porous materials with uniformly and non-uniformly distributed pores. The porous panels' material properties are distributed in the thickness direction using specific functions. The equations of motion are derived using Hamilton's principle based on trigonometrical shear deformation theory and solved by performing the Galerkin solution procedure with simply supported edge conditions. The accuracy of the obtained natural frequency equation is confirmed by comparing the results to those of previously published in literature. Under comprehensive parametric studies, the influence of porosity coefficient, porosity distribution patterns, radius-to-curve length ratio, orthotropy, and stiffness of elastic foundation parameters on the free vibration response of porous orthotropic cylindrical panels are discussed in detail.

Keywords: Porous panel, vibration, shear deformation, elastic foundation, porosity.

1. Introduction

The investigation of structural components resting on elastic foundations has attracted much attention from researchers because of their application in various engineering fields, such as footings in building construction, pavements in roadways, and aeronautical engineering. A way to solve the above problems is to incorporate the elastic behavior of foundations in the equations of motion of structural components. Winkler and Pasternak's foundations are the two elastic foundation approaches considered commonly in the literature. A Winkler foundation called a one-parameter elastic foundation is represented as a separate spring. Pasternak added a shear layer over the springs to improve the assumption [1].

The mechanical behavior of structural members is analyzed using classical plate (or shell) theory, first-order shear deformation theory, and higher-order shear deformation theory. After developing these theories, many parametric studies have been carried out on the vibration problems of plates and shells resting on elastic foundations. Zamani et al. [2] analyzed the free vibration response of laminated viscoelastic composite plates resting on a Pasternak viscoelastic medium. The composite plate comprises a linear viscoelastic matrix and isotropic elastic fibers. Duc et al. [3] investigated the nonlinear dynamic and vibration problems of spherical shells made of FG material placed on an elastic foundation in the thermal environment. Material properties are graded along the thickness using a sigmoid law. Zenkour and Radwan [4] studied the free vibration of sandwich plates resting on Pasternak foundations based on hyperbolic shear deformation theory. Using Reddy's third-order shear deformation theory, Quan and Duc [5] presented the nonlinear vibration behavior of imperfect FG double-curved shells resting on an elastic foundation. They modeled the temperature-dependent material properties through the

thickness via a power-law rule. Park and Kim [6] analyzed the natural frequencies of FG cylindrical fluid-filled shells. They assumed the shells partially rested on a Pasternak elastic foundation and material properties vary along the thickness. Ninh and Bich [7] studied the nonlinear vibration characteristics of toroidal shell segments with a ceramic-FG-metal layer surrounded by an elastic foundation based on classical shell theory. Jung et al. [8] proposed a refined-higher-order shear deformation theory for analyzing the free and forced vibration of FG plates on elastic foundations. Depending on two power-law distributions, they graded the material properties in the thickness direction. Kim [9] investigated the free vibration behavior of FG cylindrical shell partially rested on elastic foundations with an oblique edge using first-order shear deformation theory. The material properties are modeled across the thickness via a four-parameter power-law. Asanjarani et al. [10] presented the influence of geometric parameters and elastic foundations on the free vibration of two-dimensional FG truncated conical shells based on the first-order shear deformation theory. The material properties are graded in the thickness and length directions using a power-law distribution. Ahmed [11] analyzed the free vibration characteristics of a non-homogeneous orthotropic elliptical cylindrical shell resting on a non-uniform Winkler foundation. Bich et al. [12] studied the nonlinear dynamic and vibration responses of imperfect eccentrically stiffened FG double-curved shells placed on elastic foundation using first-order shear deformation theory. Thai et al. [13] proposed a simple refined shear deformation theory for analyzing the bending, buckling, and vibration behaviors of thick plates resting on the Pasternak foundation. Sobhy [14] focused on the buckling and vibration of exponentially graded sandwich plates on an elastic foundation. The sandwich plate is modeled as a fully ceramic core and exponentially graded face sheets.

Porous materials play a significant role in many fields, such as energy management, vibration control, thermal insulation, and sound absorption. Porous materials such as porous metals, ceramics, and polymer foams favor various engineering applications Kamranfard et al. [15]. These superior properties of porous materials have attracted the attention of researchers. Static and dynamic behaviors of structural components made of porous materials have been studied in recent years. Turan [16] studied the free vibration response of porous orthotropic laminated plates with trigonometric porosity distribution via higher-order shear deformation theory. Wang [17] analyzed the electro-mechanical vibration of FG porous plates with porosity distribution in the thickness direction. Porous FG material properties are graded using a modified power-law rule containing the porosity effects. Rezaei and Saidi [18] presented an exact analytical approach based on the first-order shear deformation theory for free vibration analysis of fluid-saturated porous annular sector plates. They graded the material properties in the thickness direction using a cosine function. Kamranfard et al. [15] investigated the effects of porosity and geometrical parameters on the critical buckling loads and natural frequencies of moderately thick annular plates. Based on the refined shear deformation theory, Barati and Zenkour [19] studied the electro-thermoelastic vibration of FG piezoelectric porous plates. The material properties are varied along the thickness direction depending on the modified power-law rule. Using first-order shear deformation theory, Barati [20] analyzed the natural frequencies of FG porous nanoshells with porosities evenly and unevenly distributed in the thickness direction. Wang and Wu [21] presented the free vibration response of FG porous cylindrical shell under sinusoidal shear deformation theory. They considered two types of graded porosity distribution patterns across thickness. Shojaeefard et al. [22] analyzed the influence of porosity and gradation index on the free vibration and thermal buckling behavior of micro temperature-dependent FG porous plates based on the first-order shear deformation theory. Akbaş [23] investigated FG porous plates' static and vibration analysis under first-order shear deformation theory. Porosity-dependent material properties are graded in the thickness direction via a power-law model with porosities. Rezaei and Saidi [24] discussed the porosity effect on the thick plates' free vibration response using Reddy's third-order shear deformation

theory. Material properties of porous plates are determined in the thickness direction using a cosine function.

Furthermore, the literature has reported static and dynamic analysis of porous structural components on elastic foundations in recent years. Structural members on the elastic foundation are modeled depending on the Winkler and Pasternak interactions. Demir and Turan [25] investigated the critical buckling load of porous orthotropic cylindrical panels resting on the Winkler foundation. The porosity distribution is modeled in the thickness direction using a cosine function. Kumar et al. [26] analyzed the effect of porosity parameters, porosity distribution, and elastic foundation parameters on the natural frequencies of FG porous plates with variable thickness based on first-order shear deformation theory. The porosity-dependent material properties are graded using power-law, exponential-law, and sigmoid-law rules. Tran et al. [27] analyzed the static and free vibration behavior of FG porous nanoshell resting on an elastic foundation under extended four-unknown higher-order shear deformation theory. They graded the porous FG material using uneven porosity and logarithmic-uneven porosity distributions. Balak et al. [28] studied the free vibration response of an elliptical sandwich microplate made of a saturated porous core and two piezoelectric face sheets. The microplate is on the elastic foundation, and governing equations of the problem are derived using first-order shear deformation theory. Pham et al. [29] focused on the static bending and hygro-thermo-mechanical vibration behavior of porous FG sandwich double-curved shells on the elastic foundation via the four-unknown shear deformation theory. The shells comprised a full ceramic core and two porous face layers with uneven porosity distribution. Shahverdi and Barati [30] proposed a general nonlocal elasticity model to analyze the vibration of porous nanoplates resting on the elastic foundation. Material properties are modeled via a modified power-law and Mori-Tanaka models containing the porosity effects.

By reviewing the above literature, the free vibration problem of porous orthotropic cylindrical panels resting on elastic foundations has not yet been investigated. Therefore, it is of great significance to fill the gaps in the study. Based on the trigonometrical shear deformation theory, this paper focuses on the natural frequencies of porous orthotropic cylindrical panels resting on the Pasternak foundation. Porous material properties such as Young's modulus, shear modulus, and mass density vary across the thickness via trigonometric functions. The governing equations of the problem are obtained using higher-order shear deformation theory and solved via the Galerkin solution procedure. The numerical results calculated by the present frequency equation indicate good convergence and accuracy by comparing with the literature results. The effect of porosity coefficients, porosity distribution patterns, geometrical parameters, orthotropy, and elastic foundation parameters on the free vibration response of porous orthotropic cylindrical panels are discussed in detail.

2. Theoretical Formulations

Fig. 1 shows the configuration of the porous orthotropic cylindrical panel with geometrical parameters: R is the curvature radius; s, a are the length of the curve and length in the y direction, respectively; h is the thickness. The cylindrical panel resting on the elastic foundation (EF) consists of two parameters (k_s, k_w). In which k_s is Pasternak stiffness, and k_w is Winkler stiffness.
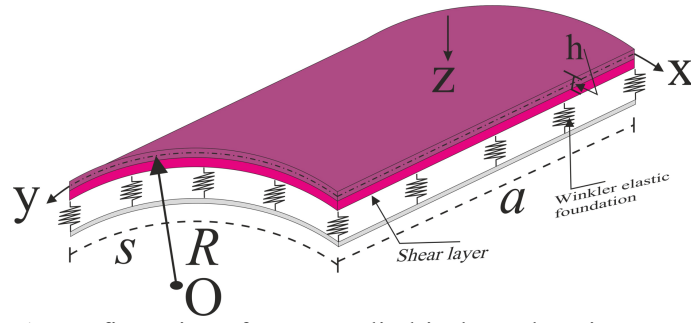
Fig. 1. Configuration of porous cylindrical panel resting on an EF

2.1. Determination of the Material Properties of the Porous Panel

This paper focuses on a non-uniform symmetric, a non-uniform asymmetric, and a uniform porosity distribution. The non-uniform symmetric porosity distribution is denoted by ND1, the non-uniform symmetric porosity distribution is abbreviated ND2, and UD indicates the uniform porosity distribution. The porosity-dependent material properties of the porous panel, including Young's modulus E, shear modulus G, and mass density ρ are varied continuously from the top surface ($z = -0.5h$) to the bottom ($z = +0.5h$) surface. The corresponding variations of material properties are given by Eqs (1)-(3) for the NDs and UD.

ND₁:

$$\left(E_i, G_j, \rho\right) = \left(E_{0i}, G_{0j}, \rho_0\right)(1 - [\eta_0, \eta_0, \eta_0^*]) \frac{3.45}{\pi} sin^2\left(\frac{\pi z}{h}\right), i = 1,2; j = 12, 13, 23 \quad (1a)$$

ND₂:

$$\left(E_i, G_j, \rho\right) = \left(E_{0i}, G_{0j}, \rho_0\right)(1 - [\eta_0, \eta_0, \eta_0^*]) \frac{3.45}{\pi} sin\left(\frac{\pi z}{h}\right), i = 1,2; j = 12, 13, 23 \quad (1b)$$

UD:

$$\left(E_i, G_j, \rho\right) = \left(E_{0i}, G_{0j}, \rho_0\right)[\hat{\eta}_0, \hat{\eta}_0, \hat{\eta}_0^*], i = 1,2; j = 12, 13, 23 \quad (1c)$$

where $0 \leq \eta_0, \hat{\eta}_0, \eta_0^*, \hat{\eta}_0^* < 1$ is the porosity coefficients and E_0, G_0 and ρ_0 are corresponding values of the material with no porosity ($\eta_0 = 0$). The porous panel's Poisson ratio (ν_{12}) is assumed to be constant along the panel thickness. Fig. 2 presents the difference between the non-uniform symmetric porosity distribution (ND_1) with the non-uniform asymmetric distribution (ND_2).

The typical mechanical properties of porous material in terms of mass density can be given as follows [31]

$$E_{max}/E_{min} = (\rho_{max}/\rho_{min})^2 \quad (2)$$

According to $\eta_0 = 1 - E_i/E_{0i}$ and $\eta_0^* = 1 - \rho/\rho_0$, the following relation can be obtained using Eq. (2):

$$\eta_0^* = 1 - \sqrt{1 - \eta_0}, \qquad \hat{\eta}_0^* = \sqrt{\hat{\eta}_0} \quad (3a)$$

Without loss of generality, the UD and ND_1 porous panels' masses are set to be equal, and the relationship between $\hat{\eta}_0$ and η_0 can be estimated using the following equation:

$$\hat{\eta}_0 = -2.7379\eta_0^6 + 6.9529\eta_0^5 - 7.0465\eta_0^4 + 3.5157\eta_0^3 - 0.9543\eta_0^2 - 0.4356\eta_0$$
$$+ 0.9949 \tag{3b}$$

(a)

(b)
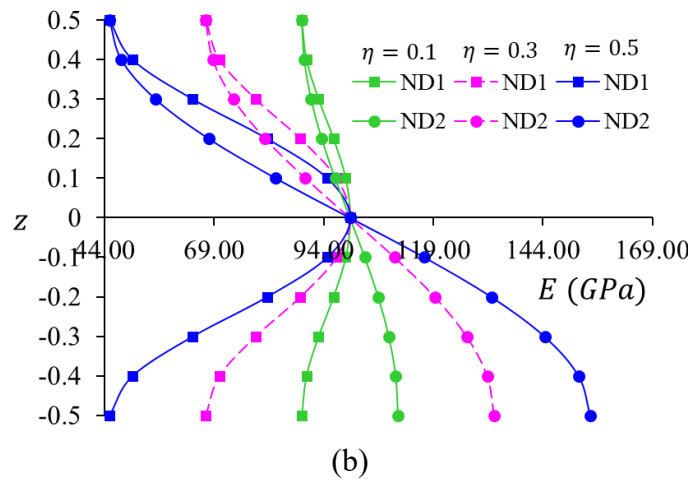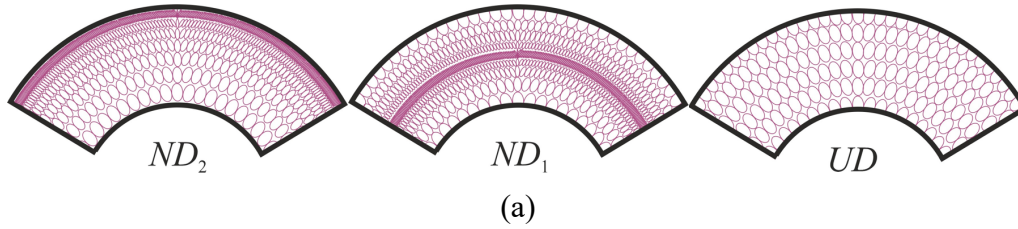
Fig. 2. (a) Three types of the porosity distribution patterns of porous material, (b) variation of Young's modulus (E_1) of the non-uniform symmetric and non-uniform asymmetric porosity distributions along the thickness direction

2.2. Kinematic Relations

This section contains the derivation of the cylindrical panel's kinematic relations. A cylindrical panel's displacement fields can be expressed based on the higher-order shear deformable plate theory as follows:

$$u_x(x, y, z, t) = u_1(x, y, t) - zu_{3,x} + \phi(z)\Gamma_x(x, y, t)$$
$$u_y(x, y, z, t) = u_2(x, y, t) - zu_{3,y} + \phi(z)\Gamma_y(x, y, t) \tag{4}$$
$$u_z(x, y, z, t) = u_3(x, y, t)$$

where u_1 and u_2 are longitudinal and transverse displacements of the mid-surface, respectively; u_3 is the deflection through the z-axis. Γ_x and Γ_y are the rotations of the cross-section about the y- and x-axis, respectively. $\phi(z)$ represents the shape function of shear deformation theory. The following equation defines the nonzero strains of the panel:

$$\varepsilon_{xx} = \varepsilon_{xx}^0 - z\varepsilon_{xx}^1 + \phi(z)\varepsilon_{xx}^2, \varepsilon_{yy} = \varepsilon_{yy}^0 - z\varepsilon_{yy}^1 + \phi(z)\varepsilon_{yy}^2 \tag{5}$$

$$\gamma_{xy} = \gamma_{xy}^0 - z\gamma_{xy}^1 + \phi(z)\gamma_{xy}^2, \gamma_{xz} = \varphi(z)\Gamma_x(x,y,t), \gamma_{yz} = \varphi(z)\Gamma_y(x,y,t)$$

where

$$
\begin{aligned}
&\varepsilon_{xx}^0 = u_{1,x} - u_3\widehat{R}, \varepsilon_{yy}^0 = u_{2,y}, \gamma_{xy}^0 = u_{1,y} + u_{2,x} \\
&\varepsilon_{xx}^1 = u_{3,xx}, \varepsilon_{yy}^1 = u_{3,yy}, \varepsilon_{xy}^1 = 2u_{3,xy} \\
&\varepsilon_{xx}^2 = \Gamma_{x,x}, \varepsilon_{yy}^2 = \Gamma_{y,y}, \varepsilon_{xy}^2 = \Gamma_{x,y} + \Gamma_{y,x} \\
&\varphi(z) = \phi_{,z}(z), \widehat{R} = 1/R
\end{aligned}
\tag{6}
$$

In this paper, the following shape function is considered by Ebrahimi et al. [32]:

$$\phi(z) = \frac{he^z}{h^2 + \pi^2}\left(\pi\sin\left(\frac{\pi z}{h}\right) + h\cos\left(\frac{\pi z}{h}\right)\right) - \frac{h^2}{h^2 + \pi^2} \tag{7}$$

2.3. Equations of Motion

Here, Hamilton's principle can be performed to reach the Euler–Lagrange equations of a porous orthotropic cylindrical panel. This principle can be defined in the following form:

$$\int_{t_1}^{t_2} \left(\delta u_s + \delta u_f - \delta u_k\right)dt = 0 \tag{8}$$

where δu_s, δu_f and δu_k are strain energy, elastic foundation's potential energy, and kinetic energy, respectively. The variation of strain energy can be expressed as

$$
\begin{aligned}
\delta u_s &= \int_V^0 \left(\sigma_{xx}\delta\varepsilon_{xx} + \sigma_{yy}\delta\varepsilon_{yy} + \tau_{xy}\delta\gamma_{xy} + \tau_{xz}\delta\gamma_{xz} + \tau_{yz}\delta\gamma_{yz}\right)dV \\
&= \int_0^a \int_0^b \left(
\begin{array}{l}
N_{xx}\delta\varepsilon_{xx}^0 + N_{yy}\delta\varepsilon_{yy}^0 + N_{xy}\delta\gamma_{xy}^0 + M_{xx}\delta\varepsilon_{xx}^1 + M_{yy}\delta\varepsilon_{yy}^1 + M_{xy}\delta\gamma_{xy}^1 \\
+ P_{xx}\delta\varepsilon_{xx}^2 + P_{yy}\delta\varepsilon_{yy}^2 + P_{xy}\delta\gamma_{xy}^2 + N_{xz}\varepsilon_{xx}^2 + N_{yz}\varepsilon_{yy}^2
\end{array}
\right)dxdy
\end{aligned}
\tag{9}
$$

In Eq. (9), the axial forces, bending moments, higher-order moments, and shear forces can be defined as:

$$(N_i, M_i, P_i) = \int_{-0.5h}^{0.5h} (1, z, \phi(z))\sigma_i, i = xx, yy,$$

$$(N_j, M_j, P_j) = \int_{-0.5h}^{0.5h} (1, z, \phi(z))\tau_j, j = xy,$$

$$\tag{10}$$

$$N_k = \int_{-0.5h}^{0.5h} \varphi(z)\tau_k, k = xz, yz$$

The variation of the elastic foundation's potential energy can be determined as:

$$\delta u_f = \int_0^a \int_0^b \left(k_w u_3 - k_s(u_{3,xx} + u_{3,yy}) \right) \delta u_3 \, dxdy \tag{11}$$

The first variation of kinetic energy can be expressed as:

$$\begin{aligned}
\delta u_k &= \int_V \rho(\dot{u}_x \delta \dot{u}_x + \dot{u}_y \delta \dot{u}_y + \dot{u}_z \delta \dot{u}_z) \, dV \\
&= I_0 \int_0^a \int_0^b (\dot{u}_1 \delta \dot{u}_1 + \dot{u}_2 \delta \dot{u}_2 + \dot{u}_3 \delta \dot{u}_3) dxdy + I_1 \int_0^a \int_0^b (\dot{u}_{3,x} \delta \dot{u}_{3,x} + \dot{u}_{3,y} \delta \dot{u}_{3,y}) dxdy \\
&+ I_2 \int_0^a \int_0^b (\dot{\Gamma}_{x,x} \delta \dot{\Gamma}_{x,x} + \dot{\Gamma}_{y,y} \delta \dot{\Gamma}_{y,y}) dxdy
\end{aligned} \tag{12}$$

In all the equations, the dot-superscript denotes the differentiation with respect to time, and the mass inertias used in the above equations are given in the following form:

$$(I_0, I_1, I_2) = \int_{-0.5h}^{0.5h} \rho(1, z^2, [\phi(z)]^2) dz \tag{13}$$

By substituting Eqs. (9), (11), and (12) into Eq. (8) and setting the coefficients of δu_1, δu_2, δu_3, $\delta \Gamma_x$, and $\delta \Gamma_y$ to zero, the Euler–Lagrange equations of porous orthotropic cylindrical panels can be obtained as:

$$N_{xx,x} + N_{xy,y} = I_0 \ddot{u}_1 \tag{14a}$$

$$N_{xy,x} + N_{yy,y} = I_0 \ddot{u}_2 \tag{14b}$$

$$\hat{R}N_{xx} + M_{xx,xx} + 2M_{xy,xy} + M_{yy,yy} - k_w u_3 + k_s(u_{3,xx} + u_{3,yy})$$
$$= I_0 \ddot{u}_3 - I_1(\ddot{u}_{3,xx} + \ddot{u}_{3,yy}) \tag{14c}$$

$$P_{xx,x} + P_{xy,y} - N_{xz} = I_2 \ddot{\Gamma}_x \tag{14d}$$

$$P_{xy,x} + P_{yy,y} - N_{yz} = I_2 \ddot{\Gamma}_y \tag{14e}$$

The inertial forces $I_0 \ddot{u}_1$ and $I_0 \ddot{u}_2$ are assumed to be negligible in light of the assumption of $(u_1, u_2) \ll u_3$. By deriving Eqs. (14a) and (14d) with respect to x, and Eqs. (14b) and (14e) with respect to y gives us:

$$N_{xx,xx} + N_{xy,xy} = 0 \tag{15a}$$

$$N_{xy,xy} + N_{yy,yy} = 0 \tag{15b}$$

$$\hat{R}N_{xx} + M_{xx,xx} + 2M_{xy,xy} + M_{yy,yy} - k_w u_3 + k_s\left(u_{3,xx} + u_{3,yy}\right)$$
$$= I_0\ddot{u}_3 - I_1\left(\ddot{u}_{3,xx} + \ddot{u}_{3,yy}\right) \tag{15c}$$

$$P_{xx,xx} + P_{xy,xy} - N_{xz,x} = I_2\ddot{\Gamma}_{x,x} \tag{15d}$$

$$P_{xy,xy} + P_{yy,yy} - N_{yz,y} = I_2\ddot{\Gamma}_{y,y} \tag{15e}$$

2.4. Stress-Strain Relations

The stress-strain relations of a porous orthotropic cylindrical panel can be written as the following equation using Hooke's law.

$$\sigma_{xx} = e_{11}\varepsilon_{xx} + e_{12}\varepsilon_{yy}; \; \sigma_{yy} = e_{12}\varepsilon_{xx} + e_{22}\varepsilon_{yy}; \; \tau_{yz} = e_{44}\gamma_{yz}; \; \tau_{xz} = e_{55}\gamma_{xz};$$
$$\tau_{xy} = e_{66}\gamma_{xy} \tag{16}$$

where

$$e_{11} = \frac{E_1}{1 - \nu_{12}\nu_{21}}, e_{12} = \frac{\nu_{21}E_1}{1 - \nu_{12}\nu_{21}}, e_{22} = \frac{E_2}{1 - \nu_{12}\nu_{21}}, e_{44} = G_{23}, e_{55} = G_{13},$$
$$e_{66} = G_{12} \tag{17}$$

Substituting Eqs. (5), (6), and (16) into Eq. (10) gives the following equation:

$$N_{xx} = A_{11}u_{1,x} + A_{12}u_{2,y} - B_{11}u_{3,xx} - B_{12}u_{3,yy} + C_{11}\Gamma_{x,x} + C_{12}\Gamma_{y,y}$$
$$N_{yy} = A_{12}u_{1,x} + A_{22}u_{2,y} - B_{12}u_{3,xx} - B_{22}u_{3,yy} + C_{12}\Gamma_{x,x} + C_{22}\Gamma_{y,y}$$
$$N_{xy} = A_{66}u_{1,y} + A_{66}u_{2,x} - 2B_{66}u_{3,xy} + C_{66}\Gamma_{x,y} + C_{66}\Gamma_{y,x} \tag{18a}$$

$$M_{xx} = B_{11}u_{1,x} + B_{12}u_{2,y} - D_{11}u_{3,xx} - D_{12}u_{3,yy} + E_{11}\Gamma_{x,x} + E_{12}\Gamma_{y,y}$$
$$M_{yy} = B_{12}u_{1,x} + B_{22}u_{2,y} - D_{12}u_{3,xx} - D_{22}u_{3,yy} + E_{12}\Gamma_{x,x} + E_{22}\Gamma_{y,y}$$
$$M_{xy} = B_{66}u_{1,y} + B_{66}u_{2,x} - 2D_{66}u_{3,xy} + E_{66}\Gamma_{x,y} + E_{66}\Gamma_{y,x} \tag{18b}$$

$$P_{xx} = C_{11}u_{1,x} + C_{12}u_{2,y} - E_{11}u_{3,xx} - E_{12}u_{3,yy} + F_{11}\Gamma_{x,x} + F_{12}\Gamma_{y,y}$$
$$P_{yy} = C_{12}u_{1,x} + C_{22}u_{2,y} - E_{12}u_{3,xx} - E_{22}u_{3,yy} + F_{12}\Gamma_{x,x} + F_{22}\Gamma_{y,y}$$
$$P_{xy} = C_{66}u_{1,y} + C_{66}u_{2,x} - 2E_{66}u_{3,xy} + F_{66}\Gamma_{x,y} + F_{66}\Gamma_{y,x} \tag{18c}$$

$$N_{xz} = D_{55}\Gamma_x$$
$$N_{yz} = D_{44}\Gamma_y \tag{18d}$$

in which

$$[A_i, B_i, C_i, D_i, E_i, F_i] = \int_{-0.5h}^{0.5h} [1, z, \phi(z), z^2, z\phi(z), [\phi(z)]^2]e_i dz, i = 11,12,22,66 \tag{19}$$

$$[D_j] = \int\limits_{-0.5h}^{0.5h} [\varphi(z)]^2 e_j dz \, , j = 44,55$$

2.5. Governing Equations

The inertial forces caused by Γ_x and Γ_y rotations in Eqs. (15d) and (15e) are minimal, so they are negligible. Substituting Eq. (18) into Eq. (15) gives the following partial differential governing equations:

$$A_{11}u_{1,xxx} + A_{66}u_{1,xyy} + (A_{12} + A_{66})u_{2,xxy} - B_{11}u_{3,xxxx} - (B_{12} + 2B_{66})u_{3,xxyy}$$
$$+ C_{11}\Gamma_{x,xxx} + C_{66}\Gamma_{x,xyy} + (C_{12} + C_{66})\Gamma_{y,xxy} = 0 \tag{20a}$$

$$(A_{12} + A_{66})u_{1,xyy} + A_{22}u_{2,yyy} + A_{66}u_{2,xxy} - (B_{12} + 2B_{66})u_{3,xxyy} - B_{22}u_{3,yyyy}$$
$$+ (C_{12} + C_{66})\Gamma_{x,xyy} + C_{22}\Gamma_{y,yyy} + C_{66}\Gamma_{y,xxy} = 0 \tag{20b}$$

$$B_{11}u_{1,xxx} + (B_{12} + 2B_{66})(u_{1,xyy} + u_{2,xxy}) + B_{22}u_{2,yyy} - D_{11}u_{3,xxxx}$$
$$- 2(D_{12} + 2D_{66})u_{3,xxyy} - D_{22}u_{3,yyyy} + E_{11}\Gamma_{x,xxx}$$
$$+ (E_{12} + 2E_{66})(\Gamma_{x,xyy} + \Gamma_{y,xxy}) + E_{22}\Gamma_{y,yyy}$$
$$+ \hat{R}(A_{11}u_{1,x} + A_{12}u_{2,y} - B_{11}u_{3,xx} - B_{12}u_{3,yy} + C_{11}\Gamma_{x,x} + C_{12}\Gamma_{y,y})$$
$$- k_w u_3 + k_s(u_{3,xx} + u_{3,yy}) - I_0\ddot{u}_3 + I_1(\ddot{u}_{3,xx} + \ddot{u}_{3,yy}) = 0 \tag{20c}$$

$$C_{11}u_{1,xxx} + C_{66}u_{1,xyy} + (C_{12} + C_{66})u_{2,xxy} - E_{11}u_{3,xxxx} - (E_{12} + 2E_{66})u_{3,xxyy}$$
$$+ F_{11}\Gamma_{x,xxx} + F_{66}\Gamma_{x,xyy} + (F_{12} + F_{66})\Gamma_{y,xxy} - D_{55}\Gamma_{x,x} = 0 \tag{20d}$$

$$(C_{12} + C_{66})u_{1,xyy} + C_{22}u_{2,yyy} + C_{66}u_{2,xxy} - (E_{12} + 2E_{66})u_{3,xxyy} - E_{22}u_{3,yyyy}$$
$$+ (F_{12} + F_{66})\Gamma_{x,xyy} + F_{22}\Gamma_{y,yyy} + F_{66}\Gamma_{y,xxy} - D_{44}\Gamma_{y,y} = 0 \tag{20e}$$

3. Solution Technique

Here, an analytical solution of the governing equations for free vibration of a porous orthotropic cylindrical panel with simply supported edges is presented. The boundary conditions for simply supported edges are given as follows:

$$u_3 = M_{xx} = \Gamma_y = 0 \ \ at \ x = 0, a$$
$$u_3 = M_{yy} = \Gamma_x = 0 \ \ at \ y = 0, b \tag{21}$$

The displacement fields are presented in the following form to satisfy the above boundary conditions:

$$u_1 = u_{11}cos(\lambda_1 x) sin(\lambda_2 y) e^{i\omega t}, u_2 = u_{22}sin(\lambda_1 x)cos(\lambda_2 y)e^{i\omega t}$$
$$u_3 = u_{33}sin(\lambda_1 x) sin(\lambda_2 y) e^{i\omega t}, \Gamma_x = u_{44}cos(\lambda_1 x)sin(\lambda_2 y)e^{i\omega t} \tag{22}$$

$$\Gamma_y = u_{55} \sin(\lambda_1 x) \cos(\lambda_2 y) e^{i\omega t}$$

where $(u_{11}, u_{22}, u_{33}, u_{44}, u_{55})$ are the unknown coefficients $(\lambda_1 = m\pi/s, \ \lambda_2 = n\pi/a)$. Substituting Eq. (22) into Eq. (20) and then utilizing the Galerkin solution procedure leads to:

$$K_{11}u_{11} + K_{12}u_{22} + K_{13}u_{33} + K_{14}u_{44} + K_{15}u_{55} = 0$$
$$K_{21}u_{11} + K_{22}u_{22} + K_{23}u_{33} + K_{24}u_{44} + K_{25}u_{55} = 0$$
$$K_{31}u_{11} + K_{32}u_{22} + K_{33}u_{33} + K_{34}u_{44} + K_{35}u_{55} - \widehat{K}_{33}\omega^2 u_{33} = 0 \qquad (23)$$
$$K_{41}u_{11} + K_{42}u_{22} + K_{43}u_{33} + K_{44}u_{44} + K_{45}u_{55} = 0$$
$$K_{51}u_{11} + K_{52}u_{22} + K_{53}u_{33} + K_{54}u_{44} + K_{55}u_{55} = 0$$

where

$$K_{11} = \frac{sa}{4}(\lambda_1^3 A_{11} + \lambda_1 \lambda_2^2 A_{66}); \ K_{12} = \frac{sa}{4}\lambda_1^2 \lambda_2 (A_{12} + A_{66});$$

$$K_{13} = -\frac{sa}{4}\left(\lambda_1^4 B_{11} + \lambda_1^2 \lambda_2^2 (B_{12} + 2B_{66})\right); \ K_{14} = \frac{sa}{4}(\lambda_1^3 C_{11} + \lambda_1 \lambda_2^2 C_{66});$$

$$K_{15} = \frac{sa}{4}\lambda_1^2 \lambda_2 (C_{12} + C_{66}); \ K_{21} = \frac{sa}{4}\lambda_1 \lambda_2^2 (A_{12} + A_{66});$$

$$K_{22} = \frac{sa}{4}(\lambda_1^2 \lambda_2 A_{66} + \lambda_2^3 A_{22}); \ K_{23} = -\frac{sa}{4}(\lambda_1^2 \lambda_2^2 (B_{12} + 2B_{66}) + \lambda_2^4 B_{22});$$

$$K_{24} = \frac{sa}{4}\lambda_1 \lambda_2^2 (C_{12} + C_{66}); \ K_{25} = \frac{sa}{4}(\lambda_1^2 \lambda_2 C_{66} + \lambda_2^3 C_{22});$$

$$K_{31} = \frac{sa}{4}\left(\lambda_1^3 B_{11} + \lambda_1 \lambda_2^2 (B_{12} + 2B_{66}) - \lambda_1 A_{11}\widehat{R}\right);$$

$$K_{32} = \frac{sa}{4}\left(\lambda_1^2 \lambda_2 (B_{12} + 2B_{66}) + \lambda_2^3 B_{22} - \lambda_2 A_{12}\widehat{R}\right);$$

$$K_{33} = -\frac{sa}{4}\left(\lambda_1^4 D_{11} + 2\lambda_1^2 \lambda_2^2 (D_{12} + 2D_{66}) + \lambda_2^4 D_{22} - (\lambda_1^2 B_{11} + \lambda_2^2 B_{12})\widehat{R} + k_w\right.$$

$$\left. + k_s(\lambda_1^2 + \lambda_2^2)\right); \ K_{34} = \frac{sa}{4}\left(\lambda_1^3 E_{11} + \lambda_1 \lambda_2^2 (E_{12} + 2E_{66}) - \lambda_1 C_{11}\widehat{R}\right); \qquad (24)$$

$$K_{35} = \frac{sa}{4}\left(\lambda_1^2 \lambda_2 (E_{12} + 2E_{66}) + \lambda_2^3 E_{22} - \lambda_2 C_{12}\widehat{R}\right);$$

$$\widehat{K}_{33} = -\frac{sa}{4}\left(I_0 + I_1(\lambda_1^2 + \lambda_2^2)\right); \ K_{41} = \frac{sa}{4}(\lambda_1^3 C_{11} + \lambda_1 \lambda_2^2 C_{66});$$

$$K_{42} = \frac{sa}{4}\lambda_1^2 \lambda_2 (C_{12} + C_{66}); \ K_{43} = -\frac{sa}{4}\left(\lambda_1^4 E_{11} + \lambda_1^2 \lambda_2^2 (E_{12} + 2E_{66})\right);$$

$$K_{44} = \frac{sa}{4}(\lambda_1^3 F_{11} + \lambda_1 \lambda_2^2 F_{66} + \lambda_1 D_{55}); \ K_{45} = \frac{sa}{4}\lambda_1^2 \lambda_2 (F_{12} + F_{66});$$

$$K_{51} = \frac{sa}{4}\lambda_1 \lambda_2^2 (C_{12} + C_{66}); \ K_{52} = \frac{sa}{4}(\lambda_1^2 \lambda_2 C_{66} + \lambda_2^3 C_{22});$$

$$K_{53} = -\frac{sa}{4}(\lambda_1^2 \lambda_2^2 (E_{12} + 2E_{66}) + \lambda_2^4 E_{22}); \ K_{54} = \frac{sa}{4}\lambda_1 \lambda_2^2 (F_{12} + F_{66});$$

$$K_{55} = \frac{sa}{4}(\lambda_1^2 \lambda_2 F_{66} + \lambda_2^3 F_{22} + \lambda_2 D_{44})$$

By obtaining the determinant of the coefficient matrix of the following equation and setting this multinomial to zero, we can obtain Eq. (26):

$$\begin{bmatrix} K_{11} & K_{12} & K_{13} & K_{14} & K_{15} \\ K_{21} & K_{22} & K_{23} & K_{24} & K_{25} \\ K_{31} & K_{32} & K_{33} - \omega^2 \widehat{K}_{33} & K_{34} & K_{35} \\ K_{41} & K_{42} & K_{43} & K_{44} & K_{45} \\ K_{51} & K_{52} & K_{53} & K_{54} & K_{55} \end{bmatrix} \begin{Bmatrix} u_{11} \\ u_{22} \\ u_{33} \\ u_{44} \\ u_{55} \end{Bmatrix} = 0 \tag{25}$$

$$K_{31}\alpha_{31} + K_{32}\alpha_{32} + \left(K_{33} - \omega^2 \widehat{K}_{33}\right)\alpha_{33} + K_{34}\alpha_{34} + K_{35}\alpha_{35} = 0 \tag{26}$$

where $\alpha_{3j}(j = 1,2,..,5)$ are cofactors of the matrix in Eq. (25) and are presented in Appendix A. The porous orthotropic cylindrical panel's natural frequency can be obtained as follows:

$$\omega = \sqrt{(K_{31}\alpha_{31} + K_{32}\alpha_{32} + K_{33}\alpha_{33} + K_{34}\alpha_{34} + K_{35}\alpha_{35})/\widehat{K}_{33}\alpha_{33}} \tag{27}$$

4. Numerical Results and Discussions

In this section, the results are validated by comparing the obtained results with those of isotropic plates resting on the Pasternak foundation reported by Akhavan et al. [33] in Table 1 and those of porous isotropic cylindrical panel presented by Talebizadehsardari et al. [34] in Table 2. Then, the effect of porosity coefficients, porosity distribution patterns, orthotropy, geometrical parameters, and EF stiffness on the natural frequencies of porous orthotropic cylindrical panels resting on EF will be investigated. The non-dimensional parameters can be given as the relation in Eq. (28):

$$\widehat{\omega} = \omega s^2 \sqrt{\rho_0 h / D_0}; \ D_0 = E_1 h^3 / 12(1 - \nu_{12}\nu_{21}); \ \widehat{k}_w = k_w s^4 / D_0; \ \widehat{k}_s = k_s s^2 / D_0 \tag{28}$$

By studying Tables 1-2, it is found that the non-dimensional natural frequencies obtained in the present study are in good agreement with the results reported in the literature and thus validate the proposed solution method.

Table 1. The fundamental frequency $\widehat{\omega}$ for isotropic ($\nu_{12} = \nu_{21} = 0.3$) square plate ($\widehat{R} \to 0$).

	$\widehat{k}_w, \widehat{k}_s$					
	Akhavan et al. [33]			Present		
s/h	$(0,0)$	$(10^2, 10^1)$	$(10^3, 10^2)$	$(0,0)$	$(10^2, 10^1)$	$(10^3, 10^2)$
5	17.5055	24.3074	56.0359	17.1126	23.9139	55.5262
10	18.0840	25.6368	57.3969	19.0415	25.5961	57.3444
1000	19.7391	26.2112	57.9961	19.7426	26.2138	57.9973

Table 2. The fundamental natural frequency $\bar{\omega} = (\omega a^2 / h)\sqrt{\rho/E}$ for the *UD* cylindrical panels ($E = 70\ GPa, \nu = 0.3, \rho = 2702\ kg/m^3, h = 0.2\ m, R = 1.93\ m, s = 1.011\ m, a = 1\ m$).

η_0	Talebizadehsardari et al. [34]	Present
0	5.3650	5.3598
0.2	5.1815	5.2104
0.4	4.9651	5.0314

4.1. Natural Vibration Analysis

The following study analyzes the natural vibration of the porous orthotropic cylindrical panel with three porosity distribution patterns. The material properties of the orthotropic cylindrical panel are selected as $E_{01} = 53.78\ GPa$, $E_{02} = 17.93\ GPa$, $G_{012} = G_{013} = 8.96\ GPa$, $G_{023} = 3.45\ GPa$, $\nu_{12} = 0.25$, $\rho_0 = 1900\ kgm^{-3}$.

Table 3 and Fig. 4 report the non-dimensional fundamental natural frequencies of porous orthotropic cylindrical panels with various porosity coefficients, EF stiffness, and porosity distribution patterns at $s/h = 50$, $s/a = 1$, $R/s = 5$. The fundamental natural frequency decreases with increasing porosity coefficient for all porosity distribution patterns. The enormous and minor frequencies are obtained for ND_2 and ND_1 patterns. The most significant porosity effect is obtained in ND_1 cylindrical panels. With increasing porosity coefficient from 0 to 0.9, the ND_1 pattern effect on the fundamental natural frequencies increases as (27%), (16%), and (7.5%) for no foundation, Winkler foundation, and Pasternak foundation, respectively. With an increasing porosity coefficient from 0 to 0.9 at no foundation case, the ND_1 pattern effect on the fundamental natural frequencies increases (12%) and (16%) compared to the UD and ND_2 patterns.

Table 3. Variation of cylindrical panel's non-dimensional fundamental natural frequency with different foundation parameters, porosity coefficient, and distribution patterns.

| $\hat{k}_w, \hat{k}_s$								
0,0			60,0			60,4		
η_0	UD	ND_1	ND_2	UD	ND_1	ND_2	UD	ND_1	ND_2
0	17.904	17.904	17.904	19.507	19.507	19.507	21.434	21.434	21.434
0.1	17.651	17.453	17.964	19.320	19.139	19.562	21.318	21.154	21.484
0.2	17.383	16.977	17.935	19.125	18.758	19.535	21.201	20.872	21.460
0.3	17.095	16.471	17.816	18.921	18.362	19.426	21.085	20.588	21.361
0.4	16.786	15.932	17.606	18.708	17.952	19.233	20.970	20.306	21.185
0.5	16.447	15.355	17.300	18.481	17.528	18.954	20.858	20.032	20.932
0.6	16.070	14.735	16.895	18.240	17.096	18.585	20.751	19.777	20.599
0.7	15.644	14.067	16.382	17.980	16.663	18.120	20.655	19.561	20.180
0.8	15.131	13.352	15.750	17.689	16.260	17.550	20.576	19.434	19.670
0.9	14.415	12.626	14.984	17.329	15.983	16.867	20.543	19.540	19.063
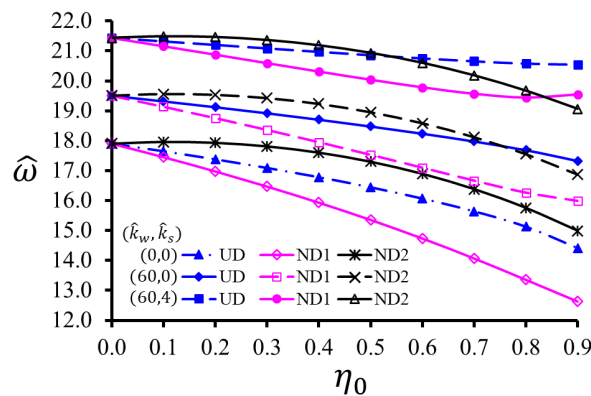
Fig. 4. Variation of non-dimensional fundamental frequency versus porosity coefficients for various elastic foundation stiffness

In the same case, the most significant ND_2 pattern effect is (5.2%) compared to the UD pattern at $\eta_0 = 0.5$. Depending on the rising porosity coefficient from 0 to 0.9, the Winkler foundation effect on the fundamental natural frequencies increases (11.3%), (17.6%), and (3.6%) for UD, ND_1, and ND_2 patterns, respectively. In the same case, the influence of the Pasternak foundation increases (22.8%), (35%), and (7.5%) for UD, ND_1, and ND_2 patterns, respectively.

Figs. 5 and 6 indicate the variation of the dimensionless fundamental natural frequency of porous orthotropic cylindrical panel resting on the Winkler and Pasternak foundations for different porosity coefficients and three porosity distributions at ($s/h = 50$, $s/a = 1$, $R/s = 5$). It is known that the growth of Winkler and Pasternak stiffness leads to increasing in dimensionless fundamental frequency for all porosity coefficients. Moreover, it is found that the effect of porosity on fundamental frequencies is more considerable with no elastic foundation. In other words, the influence of porosity decreases with increasing foundation stiffness. With an increasing Winkler foundation stiffness from 0 to 150 at $\eta_0 = 0.6$, the porosity effect diminishes as (7.4%), (10.5%), and (1.4%) for *UD, ND1, and ND2* patterns, respectively. With an increasing Pasternak foundation stiffness from 0 to 15 at $\eta_0 = 0.8$, the porosity effect decreases as (6.8%), (17.2%), and (4.7%) for UD, ND1, and ND2 *patterns*, respectively. With an increasing Pasternak foundation stiffness from 0 to 15 at $\eta_0 = 0.8$, the ND1 pattern effect on the fundamental natural frequencies diminishes as (6%) compared to the UD pattern. It decreases by (8.5%) and then increases by (6.6%) compared to the ND2 pattern. Depending on the increase in the foundation stiffness, the effect of the elastic foundation on the dimensional fundamental frequencies increases as expected.
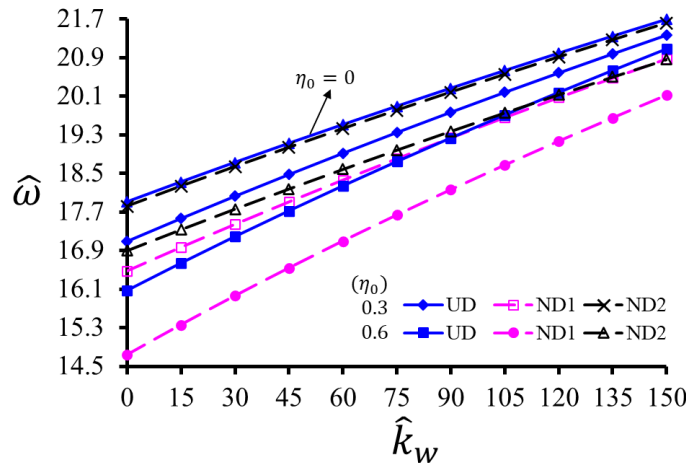
Fig. 5. Variation of non-dimensional fundamental frequency versus Winkler elastic foundation stiffness for various porosity coefficients

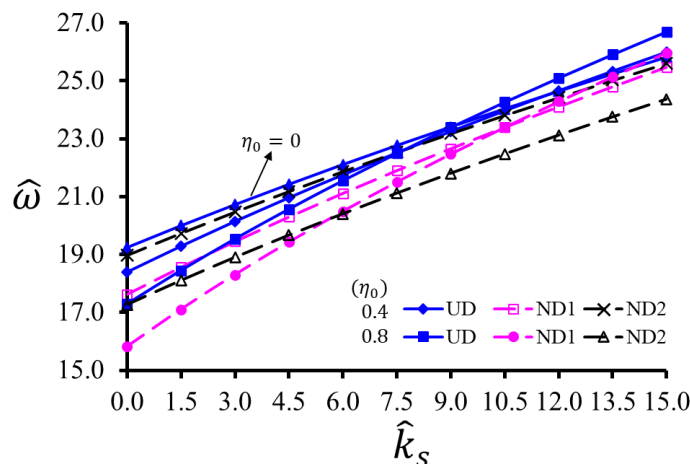Fig. 6. Variation of non-dimensional fundamental frequency versus Pasternak elastic foundation stiffness for various porosity coefficients

Fig. 7 and Table 4 show the influence of in-plane orthotropy on the free vibration behavior of porous orthotropic cylindrical panel resting on elastic foundation with respect to three porosity distributions at ($s/h = 50$, $s/a = 1$, $R/s = 5$). With an increasing orthotropy ratio from 5 to

60 at no foundation case, the porosity effect increases by (2.4%) and (5.4%) for ND_1 *and* ND_2 patterns, respectively. It remains constant at (8%) for the *UD* pattern. With an increasing orthotropy ratio from 5 to 60 at the Pasternak foundation case, the porosity effect diminishes by (1.6%) and (3.6%) for *UD and* ND_1 patterns, respectively. It increases by (1.7%) for the ND_2 pattern. With an increasing orthotropy ratio from 5 to 60 at the Pasternak foundation case, the ND_1 pattern effect on the fundamental natural frequencies diminishes by (1.5%) compared to the *UD* pattern. It decreases by (3.3%) and then increases by (2%) compared to the ND_2 pattern. Depending on the rising orthotropy ratio from 5 to 60, the Pasternak foundation effect on the fundamental natural frequencies increases (28%), (34.5%), and (28%) for *UD*, ND_1, and ND_2 patterns, respectively.

Table 4. The effect of orthotropy on the cylindrical panel's non-dimensional fundamental natural frequency with different foundation parameters, porosity coefficient, and distribution patterns.

| | $\eta_0 = 0$ | | $\eta_0 = 0.5$ | | | | | |
| | $\hat{k}_w, \hat{k}_s$ | | | | | | | |
| | 0,0 | 100,0.4 | 0,0 | | | 100,0.4 | | |
E_1/E_2	UD	UD	UD	ND_1	ND_2	UD	ND_1	ND_2
5	15.360	18.540	14.110	13.095	14.625	18.079	17.320	17.936
10	12.963	16.609	11.908	10.936	12.087	16.419	15.751	15.935
15	12.011	15.877	11.033	10.071	11.071	15.796	15.163	15.179
20	11.490	15.487	10.555	9.597	10.514	15.465	14.853	14.777
25	11.156	15.241	10.248	9.295	10.157	15.258	14.659	14.526
30	10.922	15.070	10.033	9.084	9.907	15.114	14.526	14.352
35	10.746	14.943	9.871	8.927	9.721	15.007	14.429	14.224
40	10.607	14.844	9.744	8.804	9.575	14.924	14.353	14.125
45	10.494	14.763	9.640	8.706	9.458	14.856	14.293	14.045
50	10.400	14.696	9.553	8.624	9.360	14.800	14.243	13.980
55	10.319	14.639	9.479	8.555	9.277	14.752	14.201	13.924
60	10.248	14.589	9.414	8.495	9.205	14.710	14.165	13.877
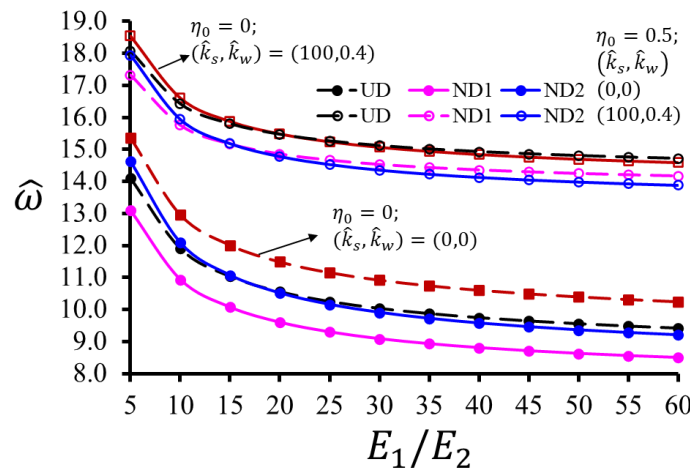
Fig. 7. Variation of non-dimensional fundamental frequency versus in-plane orthotropy ratios

To indicate the effects of the radius-to-curve length ratio on the dimensional fundamental frequency of porous orthotropic cylindrical panel resting on a Pasternak foundation for three porosity patterns, Fig. 8 and Table 5 present the fundamental frequencies versus the radius-to-curve length ratio for both perfect ($\eta_0 = 0$) and porous ($\eta_0 = 0.8$) panels. It is seen that dimensional fundamental frequencies diminish depending on the increasing radius-to-curve length ratios. The difference between *ND*s and *UD* patterns' frequency values increases with an increase in the radius-to-curve length ratio for the Pasternak foundation case. Also, the

difference between ND_1 and ND_2 patterns' frequencies increases depending on the increasing radius-to-curve length ratio for both no foundation and Pasternak foundation cases. With an increasing radius-to-curve length ratio from 0.5 to 5 at no foundation case, the porosity effect increases by (9%) and (13.5%) for ND_1 and ND_2 patterns, respectively. It remains constant at (15.5%) for the UD pattern. With an increasing radius-to-curve length ratio from 0.5 to 5 at the Pasternak foundation case, the porosity effect decreases by (3.5%) and (0.5%) for UD and ND_1 patterns, respectively. It increases by (6.3%) for the ND_2 pattern. With an increasing radius-to-curve length ratio from 0.5 to 5 at the Pasternak foundation case, the ND_1 pattern effect on the fundamental natural frequencies increases by (11%) and (4%) compared to the UD and ND_2 patterns, respectively. Depending on the rising radius-to-curve length ratio from 0.5 to 5, the Pasternak foundation effect on the fundamental natural frequencies increases (17%), (36%), and (23%) for UD, ND_1, and ND_2 patterns, respectively.

Table 5. The effect of R/s ratio on the cylindrical panel's non-dimensional fundamental natural frequency with different foundation parameters, porosity coefficient, and distribution patterns.

| | $\eta_0 = 0$ | | $\eta_0 = 0.8$ | | | | | |
| | $\hat{k}_w, \hat{k}_s$ | | | | | | | |
| | 0,0 | 75,0.5 | 0,0 | | | 75,0.5 | | |
R/s	UD	UD	UD	ND_1	ND_2	UD	ND_1	ND_2
0.5	13.141	15.907	11.105	9.930	11.932	15.357	14.638	14.924
1.0	11.232	14.370	9.492	7.813	9.372	14.234	13.293	12.968
1.5	10.842	14.067	9.162	7.355	8.749	14.016	13.029	12.526
2.0	10.702	13.960	9.044	7.187	8.497	13.939	12.935	12.351
2.5	10.636	13.910	8.989	7.108	8.366	13.903	12.892	12.261
3.0	10.601	13.882	8.959	7.065	8.289	13.884	12.868	12.209
3.5	10.579	13.866	8.940	7.039	8.238	13.872	12.854	12.174
4.0	10.565	13.855	8.929	7.022	8.203	13.864	12.844	12.150
4.5	10.556	13.848	8.920	7.010	8.177	13.859	12.838	12.133
5.0	10.549	13.843	8.915	7.002	8.157	13.855	12.833	12.119
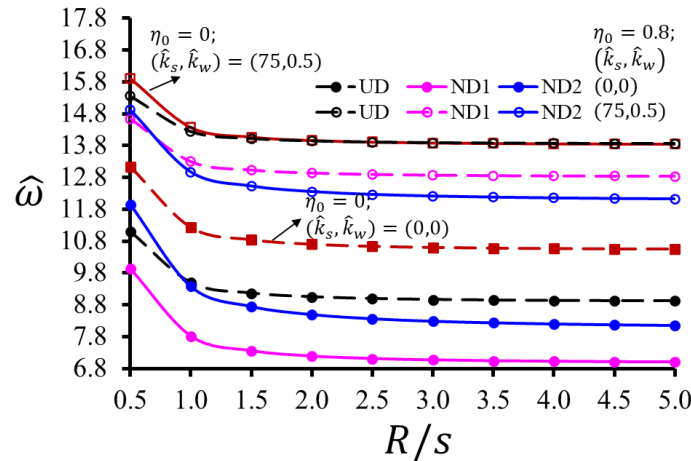
Fig. 8. Variation of non-dimensional fundamental frequency versus radius-to-curve length ratios

5. Conclusions

The paper studies the free vibration of porous orthotropic cylindrical panels resting on an elastic foundation within the higher-order shear deformation theory. Three types of porosity distributions are considered. Mechanical properties of the porous panel are modeled in the thickness direction based on specific functions. The equations of motion are derived by using

Hamilton's principle. The Galerkin solution method is used to solve governing partial differential equations. It is indicated that the vibration responses of porous orthotropic cylindrical panels are significantly affected by various parameters such as elastic foundation stiffness, porosity coefficients, porosity distribution patterns, and geometrical parameters.

This subject is a less-explored area in vibration analysis, and including porosity introduces complexities related to structure-foundation interactions. Incorporating an elastic foundation beneath the panels adds a layer of realism to the analysis. The interaction between the panel and the foundation significantly influences the panel's vibration response, making the study relevant for practical engineering applications. The utilization of shear deformation theory is a distinctive approach. This theory considers the effects of transverse shear deformation, which is particularly important for thin and composite structures like cylindrical panels. Its integration adds precision to the results compared to classical plate theories. This subject bridges structural mechanics, soil-structure interaction, and material science concepts. The novelty lies in combining these diverse fields to analyze a complex system's behavior comprehensively. The outcomes of this study can have implications for various engineering fields, such as aerospace, civil engineering, and mechanical engineering. Optimizing the design of structures with these characteristics could lead to improved performance and efficiency.

Numerical results show that:
- The ND_2 cylindrical panels' dimensional fundamental frequencies are more significant than the ND_1 ones.
- The effect of the ND_1 pattern on the fundamental frequencies is more significant than the other patterns.
- The elastic foundation effect on the fundamental frequencies increases with the rising porosity coefficient.
- The influence of porosity on the dimensionless frequencies decreases with increasing elastic foundation stiffness.
- The effect of porosity on the fundamental frequencies of cylindrical panels resting on the Pasternak foundation decreases with increasing orthotropy and radius-to-curve length ratios for UD and ND_1 patterns. It increases for the ND_2 pattern.
- The influence of porosity on the fundamental frequencies of cylindrical panels with no foundation increases with increasing orthotropy and radius-to-curve length ratios for ND_1 and ND_2 patterns. It remains constant for the UD pattern.
- The difference between ND_1 and ND_2 cylindrical panels' frequencies increases depending on the increasing radius-to-curve length ratio.

Appendix A

$$\alpha_{31} = K_{12}K_{23}(K_{44}K_{55} - K_{45}K_{54}) + K_{12}K_{43}(K_{25}K_{54} - K_{24}K_{55}) + K_{12}K_{53}(K_{24}K_{45} - K_{25}K_{44})$$
$$+K_{13}K_{45}(K_{22}K_{54} - K_{24}K_{52}) + K_{13}K_{44}(K_{25}K_{52} - K_{22}K_{55}) + K_{13}K_{42}(K_{24}K_{55} - K_{25}K_{54})$$
$$+K_{14}K_{23}(K_{45}K_{52} - K_{42}K_{55}) + K_{14}K_{22}(K_{43}K_{55} - K_{45}K_{53}) + K_{14}K_{25}(K_{42}K_{53} - K_{43}K_{52})$$
$$+K_{15}K_{53}(K_{22}K_{44} - K_{24}K_{42}) + K_{15}K_{43}(K_{24}K_{52} - K_{22}K_{54}) + K_{15}K_{23}(K_{42}K_{54} - K_{44}K_{52})$$

$$(A1)$$

$$\alpha_{32} = -K_{11}K_{23}(K_{44}K_{55} - K_{45}K_{54}) - K_{11}K_{43}(K_{25}K_{54} - K_{24}K_{55}) - K_{11}K_{53}(K_{24}K_{45} - K_{25}K_{44})$$
$$-K_{13}K_{45}(K_{21}K_{54} - K_{24}K_{51}) - K_{13}K_{44}(K_{25}K_{51} - K_{21}K_{55}) - K_{13}K_{41}(K_{24}K_{55} - K_{25}K_{54})$$
$$-K_{14}K_{23}(K_{45}K_{51} - K_{41}K_{55}) - K_{14}K_{21}(K_{43}K_{55} - K_{45}K_{53}) - K_{14}K_{25}(K_{41}K_{53} - K_{43}K_{51})$$
$$-K_{15}K_{21}(K_{44}K_{53} - K_{43}K_{54}) - K_{15}K_{41}(K_{23}K_{54} - K_{24}K_{53}) - K_{15}K_{51}(K_{24}K_{43} - K_{23}K_{44})$$

$$(A2)$$

$$\alpha_{33} = K_{11}K_{22}(K_{44}K_{55} - K_{45}K_{54}) + K_{11}K_{42}(K_{25}K_{54} - K_{24}K_{55}) + K_{11}K_{52}(K_{24}K_{45} - K_{25}K_{44})$$
$$+K_{12}K_{21}(K_{45}K_{54} - K_{44}K_{55}) + K_{12}K_{24}(K_{41}K_{55} - K_{45}K_{51}) + K_{12}K_{25}(K_{44}K_{51} - K_{41}K_{54})$$
$$+K_{14}K_{41}(K_{25}K_{52} - K_{22}K_{55}) + K_{14}K_{21}(K_{42}K_{55} - K_{45}K_{52}) + K_{14}K_{51}(K_{22}K_{45} - K_{25}K_{42})$$
$$+K_{15}K_{41}(K_{22}K_{54} - K_{24}K_{52}) + K_{15}K_{21}(K_{44}K_{52} - K_{42}K_{54}) + K_{15}K_{51}(K_{24}K_{42} - K_{22}K_{44})$$

$$(A3)$$

$$\alpha_{34} = -K_{11}K_{42}(K_{25}K_{53} - K_{23}K_{55}) - K_{11}K_{22}(K_{43}K_{55} - K_{45}K_{53}) - K_{11}K_{52}(K_{23}K_{45} - K_{25}K_{43})$$
$$-K_{12}K_{21}(K_{45}K_{53} - K_{43}K_{55}) - K_{12}K_{51}(K_{25}K_{43} - K_{23}K_{45}) - K_{12}K_{41}(K_{23}K_{55} - K_{25}K_{53})$$
$$-K_{13}K_{41}(K_{25}K_{52} - K_{22}K_{55}) - K_{13}K_{21}(K_{42}K_{55} - K_{45}K_{52}) - K_{13}K_{51}(K_{22}K_{45} - K_{25}K_{42})$$
$$-K_{15}K_{21}(K_{43}K_{52} - K_{42}K_{53}) - K_{15}K_{51}(K_{23}K_{42} - K_{22}K_{43}) - K_{15}K_{41}(K_{22}K_{53} - K_{23}K_{52})$$

$$(A4)$$

$$\alpha_{35} = K_{11}K_{22}(K_{43}K_{54} - K_{44}K_{53}) + K_{11}K_{42}(K_{24}K_{53} - K_{23}K_{54}) + K_{11}K_{52}(K_{23}K_{44} - K_{24}K_{43})$$
$$+K_{12}K_{41}(K_{23}K_{54} - K_{24}K_{53}) + K_{12}K_{21}(K_{44}K_{53} - K_{43}K_{54}) + K_{12}K_{51}(K_{24}K_{43} - K_{23}K_{44})$$
$$+K_{13}K_{51}(K_{22}K_{44} - K_{24}K_{42}) + K_{13}K_{21}(K_{42}K_{54} - K_{44}K_{52}) + K_{13}K_{41}(K_{24}K_{52} - K_{22}K_{54})$$
$$+K_{14}K_{41}(K_{22}K_{53} - K_{23}K_{52}) + K_{14}K_{21}(K_{43}K_{52} - K_{42}K_{53}) + K_{14}K_{51}(K_{23}K_{42} - K_{22}K_{43})$$

$$(A5)$$

References

[1] Pasternak, P.L., On a new method of analysis of an elastic foundation by means of two foundation constants, Gosstroyizdat, Moscow, 1954.

[2] Zamani, H.A., Aghdam, M.M., Sadighi, M., Free vibration analysis of thick viscoelastic composite plates on visco-Pasternak foundation using higher-order theory. *Composite Structures*, 182, 25-35, 2017.

[3] Duc, N.D., Quang, V.D., Anh, V.T.T., The nonlinear dynamic and vibration of the S-FGM shallow spherical shells resting on an elastic foundations including temperature effects. *International Journal of Mechanical Sciences*, 123, 54-63, 2017.

[4] Zenkour, A.M., Radwan, A.F., Free vibration analysis of multilayered composite and soft core sandwich plates resting on Winkler–Pasternak foundations. *Journal of Sandwich Structures & Materials*, 20, 169-190, 2016.

[5] Quan, T.Q., Duc, N.D., Nonlinear vibration and dynamic response of shear deformable imperfect functionally graded double-curved shallow shells resting on elastic foundations in thermal environments. *Journal of Thermal Stresses*, 39, 437-459, 2016.

[6] Park, K.J., Kim, Y.W., Vibration characteristics of fluid-conveying FGM cylindrical shells resting on Pasternak elastic foundation with an oblique edge. *Thin-Walled Structures*, 106, 407-419, 2016.

[7] Ninh, D.G., Bich, D.H., Nonlinear thermal vibration of eccentrically stiffened Ceramic-FGM-Metal layer toroidal shell segments surrounded by elastic foundation. *Thin-Walled Structures*, 104, 198-210, 2016.

[8] Jung, W.Y., Han, S.C., Park, W.T., Four-variable refined plate theory for forced-vibration analysis of sigmoid functionally graded plates on elastic foundation. *International Journal of Mechanical Sciences*, 111, 73-87, 2016.

[9] Kim, Y.W., Free vibration analysis of FGM cylindrical shell partially resting on Pasternak elastic foundation with an oblique edge. *Composites Part B: Engineering*, 70, 263-276, 2015.

[10] Asanjarani, A., Satouri, S., Alizadeh, A., Kargarnovin, M.H., Free vibration analysis of

2D-FGM truncated conical shell resting on Winkler–Pasternak foundations based on FSDT. *Proceedings of the Institution of Mechanical Engineers, Part C: Journal of Mechanical Engineering Science*, 229, 818-839, 2015.

[11] Ahmed, M.K., Effects of non-uniform Winkler foundation and non-homogeneity on the free vibration of an orthotropic elliptical cylindrical shell. *European Journal of Mechanics-A/Solids*, 49, 570-581, 2015.

[12] Bich, D.H., Duc, N.D., Quan, T.Q., Nonlinear vibration of imperfect eccentrically stiffened functionally graded double curved shallow shells resting on elastic foundation using the first order shear deformation theory. *International Journal of Mechanical Sciences*, 80, 16-28, 2014.

[13] Thai, H.-T., Park, M., Choi, D.-H., A simple refined theory for bending, buckling, and vibration of thick plates resting on elastic foundation. *International Journal of Mechanical Sciences*, 73, 40-52, 2013.

[14] Sobhy, M., Buckling and free vibration of exponentially graded sandwich plates resting on elastic foundations under various boundary conditions. *Composite Structures*, 99, 76-87, 2013.

[15] Kamranfard, M., Saidi, A., Naderi, A., Analytical solution for vibration and buckling of annular sectorial porous plates under in-plane uniform compressive loading. *Proceedings of the Institution of Mechanical Engineers, Part C: Journal of Mechanical Engineering Science*, 232, 2211-2228, 2018.

[16] Turan, F., Natural frequencies of porous orthotropic two-layered plates within the shear deformation theory. *CHALLENGE*, 9, 1-11, 2023.

[17] Wang, Y.Q., Electro-mechanical vibration analysis of functionally graded piezoelectric porous plates in the translation state. *Acta Astronautica*, 143, 263-271, 2018.

[18] Rezaei, A., Saidi, A., An analytical study on the free vibration of moderately thick fluid-infiltrated porous annular sector plates. *Journal of Vibration and Control*, 24, 4130-4144, 2018.

[19] Barati, M.R., Zenkour, A.M., Electro-thermoelastic vibration of plates made of porous functionally graded piezoelectric materials under various boundary conditions. *Journal of Vibration and Control*, 24, 1910-1926, 2018.

[20] Barati, M.R., Vibration analysis of porous FG nanoshells with even and uneven porosity distributions using nonlocal strain gradient elasticity. *Acta Mechanica*, 229, 1183-1196, 2018.

[21] Wang, Y., Wu, D., Free vibration of functionally graded porous cylindrical shell using a sinusoidal shear deformation theory. *Aerospace Science and Technology*, 66, 83-91, 2017.

[22] Shojaeefard, M.H., Googarchin, H.S., Ghadiri, M., Mahinzare, M., Micro temperature-dependent FG porous plate: Free vibration and thermal buckling analysis using modified couple stress theory with CPT and FSDT. *Applied Mathematical Modelling*, 50, 633-655, 2017.

[23] Akbaş, Ş.D., Vibration and static analysis of functionally graded porous plates. *Journal of Applied and Computational Mechanics*, 3, 199-207, 2017.

[24] Rezaei, A., Saidi, A., Exact solution for free vibration of thick rectangular plates made of porous materials. *Composite Structures*, 134, 1051-1060, 2015.

[25] Demir, Y., Turan, F., Stability of Porous Orthotropic Cylindrical Panel Resting On Winkler Foundation via Hyperbolical Shear Deformation Theory, in: 10. International Congress of

Academic Research, Bolu, 2023, pp. 124-133.

[26] Kumar, V., Singh, S., Saran, V.H., Harsha, S.P., Vibration characteristics of porous FGM plate with variable thickness resting on Pasternak's foundation. *European Journal of Mechanics-A/Solids*, 85, 104124, 2021.

[27] Tran, T.T., Tran, V.K., Pham, Q.-H., Zenkour, A.M., Extended four-unknown higher-order shear deformation nonlocal theory for bending, buckling and free vibration of functionally graded porous nanoshell resting on elastic foundation. *Composite Structures*, 264, 113737, 2021.

[28] Balak, M., Jafari Mehrabadi, S., Mohseni Monfared, H., Feizabadi, H., Free vibration behavior of an elliptical sandwich microplate, consisting of a saturated porous core and two piezoelectric face layers, standing on an elastic foundation. *Acta Mechanica*, 233, 3253-3290, 2022.

[29] Pham, Q.-H., Tran, T.T., Tran, V.K., Nguyen, P.-C., Nguyen-Thoi, T., Zenkour, A.M., Bending and hygro-thermo-mechanical vibration analysis of a functionally graded porous sandwich nanoshell resting on elastic foundation. *Mechanics of Advanced Materials and Structures*, 29, 5885-5905, 2022.

[30] Shahverdi, H., Barati, M.R., Vibration analysis of porous functionally graded nanoplates. *International Journal of Engineering Science*, 120, 82-99, 2017.

[31] Chen, Z., Qin, B., Zhong, R., Wang, Q., Free in-plane vibration analysis of elastically restrained functionally graded porous plates with porosity distributions in the thickness and in-plane directions. *The European Physical Journal Plus*, 137, 1-21, 2022.

[32] Ebrahimi, F., Dabbagh, A., Taheri, M., Vibration analysis of porous metal foam plates rested on viscoelastic substrate. *Engineering with Computers*, 37, 3727-3739, 2021.

[33] Akhavan, H., Hashemi, S.H., Taher, H.R.D., Alibeigloo, A., Vahabi, S., Exact solutions for rectangular Mindlin plates under in-plane loads resting on Pasternak elastic foundation. Part II: Frequency analysis. *Computational Materials Science*, 44, 951-961, 2009.

[34] Talebizadehsardari, P., Salehipour, H., Shahgholian-Ghahfarokhi, D., Shahsavar, A., Karimi, M., Free vibration analysis of the macro-micro-nano plates and shells made of a material with functionally graded porosity: A closed-form solution. *Mechanics Based Design of Structures and Machines*, 50, 1054-1080, 2022.